



HAL
open science

Coalescence of bubbles in a high Reynolds number confined swarm

Javier Ruiz-Rus, Patricia Ern, Véronique Roig, C. Martínez-Bazán

► **To cite this version:**

Javier Ruiz-Rus, Patricia Ern, Véronique Roig, C. Martínez-Bazán. Coalescence of bubbles in a high Reynolds number confined swarm. *Journal of Fluid Mechanics*, 2022, 944, pp.A13. 10.1017/jfm.2022.492 . hal-03719060

HAL Id: hal-03719060

<https://hal.science/hal-03719060v1>

Submitted on 10 Jul 2022

HAL is a multi-disciplinary open access archive for the deposit and dissemination of scientific research documents, whether they are published or not. The documents may come from teaching and research institutions in France or abroad, or from public or private research centers.

L'archive ouverte pluridisciplinaire **HAL**, est destinée au dépôt et à la diffusion de documents scientifiques de niveau recherche, publiés ou non, émanant des établissements d'enseignement et de recherche français ou étrangers, des laboratoires publics ou privés.

Coalescence of bubbles in a high Reynolds number confined swarm

J. Ruiz-Rus¹†, P. Ern¹, V. Roig¹ and C. Martínez-Bazán^{2,3}

¹Institut de Mécanique des Fluides de Toulouse, Université de Toulouse - CNRS, France

²Departamento de Mecánica de Estructuras e Ingeniería Hidráulica. Universidad de Granada. Campus Fuentenueva s/n, 18071, Granada, Spain

³Andalusian Institute for Earth System Research, University of Granada, Avda. del Mediterráneo s/n, 18006, Granada, Spain

(Received xx; revised xx; accepted xx)

We investigate experimentally the coalescence cascade process for a confined swarm of deformable bubbles immersed in a bidimensional vertical cell filled with water. For different gas volume fractions, air bubbles of size D_0 larger than the cell thickness are injected at the bottom of the cell. The bubbles swarms transformation is explored using high-speed visualizations. The time evolution of each bubble in the swarm is determined using a specifically developed algorithm, enabling bubble tracking and coalescence detection. We determine the evolution of the bubble size distribution downstream from the injection point, and show that the stages of the coalescence cascade are characterized by the diameter, D_{V90} , representative of the largest bubbles. The collision frequency of pairs of bubbles of sizes D_k and $D_{k'}$, $h(D_k, D_{k'})$, and their coalescence efficiency, λ , are obtained from the experiments. The efficiency is nearly constant, independently of the bubble sizes and of the gas volume fraction. Concerning collision frequency, our results reveal the existence of two different coalescence regimes depending on the capability of the bubbles to deform. Models describing $h(D_k, D_{k'})$ for both regimes are provided. They take into account the specific response of the bubble pair, which depends on the reduced diameter $D_p = 2D_k D_{k'} / (D_k + D_{k'})$, to the global swarm-induced agitation governed by D_{V90} and the gas volume fraction. In the first regime, occurring for smaller D_p , bubbles are brought together by agitation and rapidly coalesce, while for sufficiently large D_p , both bubbles are able to deform and spend more time adapting mutually their shapes before coalescing.

Key words: keywords must be chosen during the online submission process

1. Introduction

The dynamics of gas bubbles in liquids drives a wide variety of operations in the chemical process industry, mineral processing and food industry, among many other examples. It also leads the mass exchange between ocean and atmosphere and the generation of aerosols (Deane & Stokes 2002). Breakup and coalescence of bubbles is commonly present in most applications, and equipment is designed based on the understanding of the gas-liquid interaction phenomena and on the bubble's behaviour. Thus, a profound knowledge of interaction between bubbles as well as between the

† Email address for correspondence: javier.ruizrus@imft.fr

gas and the liquid phases is crucial to understand the processes and optimize their performance. Bubble fragmentation has been extensively investigated under different flow configurations, and different models have been proposed (Tsouris & Tavlarides 1994; Martínez-Bazán *et al.* 1999a; Wang *et al.* 2003; Qi *et al.* 2020, among many others), however there is still a large amount of scientific effort devoted to this topic. Coalescence is also essential to describe the dynamics and evolution of a population of bubbles. It is usually defined as a *three-step process* involving three different mechanisms (Prince & Blanch 1990; Chesters 1991). The first step consists of bringing close together the bubbles involved in the process, typically two of them. This step is controlled by the external liquid flow that induces the bubbles motion and cause them to collide. Once the bubbles are in contact, in order to coalesce, it is necessary to drain the thin liquid film separating them. The last stage initiates when the film becomes thin enough so that inter-molecular forces, such as van der Waals ones for pure fluids, become dominant, breaking the liquid film and thus making the bubbles coalesce. Considerable effort has been also devoted to better understand the underlying physics that characterizes the growth of the neck which forms just after a hole appears on the drained liquid film between coalescing bubbles or drops (Eggers *et al.* 1999; Paulsen *et al.* 2014; Anthony *et al.* 2017; Moreno Soto *et al.* 2018). It should be noted that the last stage of the drainage is very fast compared with the previous ones. Due to marked contrasts of coalescence efficiency observed when physico-chemical properties of the fluids vary, most of the coalescence studies concentrate on the drainage of the liquid film once the bubbles are sufficiently close (Marrucci 1969; Chesters & Hofman 1982; Oolman & Blanch 1986; Zhang & Thoroddsen 2008; Ghosh 2009; Huisman *et al.* 2012). This analysis of coalescence as a *three-step process* has been fruitful to build several global models combining knowledge obtained from different studies. It remains that, in a given flow configuration, steps come one after another without real discontinuity, thus the ratios of their respective life-times may vary depending on their ambiguous definition. In this sense, it can be, thus, interesting to analyse the coalescence process as a whole, using phenomenological models that avoid the complexity of describing in detail these stages. In the present work we focus on the global process, analysing the hydrodynamics controlling the bubble coalescence in a high-Reynolds number confined bubble swarm. In order to explain precisely the aim of our study we first present the modelling formalism that we adopt and the closure laws that we discuss.

The evolution of sizes of a population of bubbles is often modelled by means of a Boltzmann-type partial integro-differential conservation equation (Williams 1985),

$$\frac{\partial n}{\partial t} + \nabla \cdot (\bar{\mathbf{u}} n) + \frac{\partial (\mathcal{R} n)}{\partial v} = \dot{Q}_r + \dot{Q}_d, \quad (1.1)$$

where $n(v, \mathbf{x}, t) dv d\mathbf{x}$ is the probable number of bubbles with volume in the range dv about v in the spatial range $d\mathbf{x}$ about \mathbf{x} at time t , $\bar{\mathbf{u}}$ is the mean velocity of bubbles of volume v at location \mathbf{x} at time t , \dot{Q}_r , and \dot{Q}_d are the birth and death rates of change of the number of bubbles due to breakup and coalescence, and \mathcal{R} is the rate of change of the volume v of a bubble, which for flows with no thermal effects may be due to mass dissolution. In the present work, we do not include thermal effects and dissolution can be neglected ($\mathcal{R} = 0$) since the dissolution times are much larger than the characteristics residence time of bubbles for the bubble sizes considered. Equation (1.1) may depend on space and time if the problem is non homogeneous and unsteady. A dependence on the velocities of the bubbles can also be introduced if, for a given size, possible velocities are distributed in a large range where coalescence and breakup dominant mechanisms may vary. For simpler presentation we do not incorporate this effect in the following equations,

56 as the flow regime that we consider does not require this supplementary complexity to be
 57 represented. When neglecting changes of volume due to thermodynamical phase change,
 58 taking into account breakup as well as coalescence, this equation writes (Coulaloglou &
 59 Tavlarides 1977; Martínez-Bazán 1999; Marchisio & Fox 2013)

$$\frac{\partial n(v, \mathbf{x}, t)}{\partial t} + \nabla \cdot [n(v, \mathbf{x}, t) \bar{\mathbf{u}}(v, \mathbf{x}, t)] = \dot{Q}_c + \dot{Q}_b, \quad (1.2)$$

60 where \dot{Q}_c represents the sink or source terms of $n(v, \mathbf{x}, t)$ due to coalescence and \dot{Q}_b that
 61 due to breakup. Thus, the equation that determines the transport and the evolution of
 62 $n(v, \mathbf{x}, t)$ is the Liouville-Boltzmann's equation. It is a generalization of Smoluchowski's
 63 equation established for particle coagulation (Smoluchowski 1917), usually called the
 64 Population Balance Equation (PBE) (Williams 1985). Moments of order 0 and 1 of
 65 $n(v, \mathbf{x}, t)$ are respectively the total number of bubbles per unit volume, $N_\infty(\mathbf{x}, t)$, what-
 66 ever their sizes, and the volume fraction of the dispersed phase $\alpha(\mathbf{x}, t)$ (Ramkrishna 2000;
 67 Marchisio & Fox 2013),

$$N_\infty(\mathbf{x}, t) = \int_0^\infty n(v, \mathbf{x}, t) dv, \quad (1.3)$$

$$\alpha(\mathbf{x}, t) = \int_0^\infty v n(v, \mathbf{x}, t) dv. \quad (1.4)$$

69 The coalescence and breakup rates in equation (1.2) read

$$\dot{Q}_c(v, \mathbf{x}, t) = \frac{1}{2} \int_0^v \lambda(v - v', v') h(v - v', v') n(v - v', \mathbf{x}, t) n(v', \mathbf{x}, t) dv' - g_c(v) n(v, \mathbf{x}, t), \quad (1.5)$$

$$\text{and } \dot{Q}_b(v, \mathbf{x}, t) = \int_v^\infty f(v', v) m(v') g_b(v') n(v', \mathbf{x}, t) dv' - g_b(v) n(v, \mathbf{x}, t), \quad (1.6)$$

71 where $h(v, v')$ is the collision frequency between bubbles of volumes v and v' ; $\lambda(v, v')$ is
 72 the collision efficiency between bubbles of volumes v and v' ; $g_c(v)$ is the coalescence rate
 73 of bubbles of volume v with any other bubble; $g_b(v)$ is the breakup or fragmentation
 74 frequency of bubbles of volume v ; $m(v)$ the number of bubbles resulting from the
 75 fragmentation of bubbles of volume v ; and $f(v', v)$ the bubble size distribution of daughter
 76 bubbles resulting from the fragmentation of a mother bubble of volume v' . In equation
 77 (1.5), the first integral term in the r.h.s. is a source term and the second one a sink
 78 term, both due to coalescence. Similarly, in equation (1.6) source and sink terms due
 79 to fragmentation also contribute to the evolution of the population of bubbles. As a
 80 complement to equation (1.5), the coalescence rate of bubbles of volume v with any
 81 other bubble is defined by

$$g_c(v) = \int_0^\infty \lambda(v, v') h(v, v') n(v', \mathbf{x}, t) dv'. \quad (1.7)$$

82 Several closure laws and models for each of these terms have been proposed in the
 83 past. Their validity is most often limited to given hydrodynamical regimes of breakup
 84 and coalescence enforced by turbulent agitation or by mean shear flow. Sometimes they
 85 also include the influence of physico-chemical properties of the liquid or of the interface.
 86 Large amount of information on the adopted models can be found in references such
 87 as Coulaloglou & Tavlarides (1977); Prince & Blanch (1990); Chesters (1991); Martínez-
 88 Bazán *et al.* (2010) or in literature reviews such as Kolev (1993); Lasheras *et al.* (2002);
 89 Liao & Lucas (2009, 2010). However, the present work is focused on the coalescence

90 processes of bubbles rising in liquid initially at rest, leaving breakage out of its scope.
 91 Thus, without including bubble breakup, equation (1.2) reduces to,

$$\begin{aligned} \frac{\partial n(v, \mathbf{x}, t)}{\partial t} + \nabla \cdot [n(v, \mathbf{x}, t) \bar{\mathbf{u}}(v, \mathbf{x}, t)] = \\ \frac{1}{2} \int_0^v \lambda(v - v', v') h(v - v', v') n(v - v', \mathbf{x}, t) n(v', \mathbf{x}, t) dv' \quad (1.8) \\ - \int_0^\infty \lambda(v, v') h(v, v') n(v, \mathbf{x}, t) n(v', \mathbf{x}, t) dv'. \end{aligned}$$

92 In the literature there are two types of models that have been proposed for $h(v, v')$, or
 93 for the coalescence time, including phenomenological and physical models. The physical
 94 models are mainly focused on the description of the drainage process of the liquid
 95 film separating two bubbles when they get close enough (Chesters & Hofman 1982;
 96 Oolman & Blanch 1986; Ghosh 2009; Huisman *et al.* 2012). They are thus limited to
 97 coalescence in stagnant liquids unperturbed by bubbles approach motion. In contrast,
 98 the phenomenological models are introduced for moving bubbles and are based on models
 99 of collision of molecules applied in physical gas dynamics (Coulaloglou & Tavlarides 1977;
 100 Sovova 1981; Prince & Blanch 1990; Tsouris & Tavlarides 1994). In these models, the
 101 coalescence rate of bubbles of volume v with any other bubble, defined by equation (1.7),
 102 is commonly reduced to the product between a collision frequency times a coalescence
 103 efficiency.

104 The objective of this work is to determine $\lambda(v, v')$ and $h(v, v')$ from bubble coalescence
 105 experiments performed in a high-Reynolds number swarm of bubbles injected at the
 106 bottom of a planar vertical thin-gap cell filled with liquid at rest, and analyze their
 107 contribution to $g_c(v)$. This confined configuration favours observation of coalescence.
 108 Starting from injection, the bubbles are greater than the gap thickness, favoring their in-
 109 teraction since the bubbles cannot escape out of the plane. Thus, coalescence is enhanced,
 110 being the coalescence rate larger than in the three-dimensional configuration (Lundin &
 111 McCready 2009).

112 In the regime explored here, there is no dewetting of the liquid films between the
 113 bubbles and the walls, and bubbles move at large Bond and Archimedes (or Reynolds)
 114 numbers. Thus, the cascade of sizes generated by coalescence is expected to create a
 115 complex self-induced gravity-driven agitation in the swarm. Indeed, for isolated bubbles,
 116 it is already known that bubbles whose sizes vary in a range similar to the one that we
 117 observe, exhibit contrasted oscillating paths and shapes (Kelley & Wu 1997; Roig *et al.*
 118 2012; Filella *et al.* 2015; Piedra *et al.* 2015; Hashida *et al.* 2019; Pavlov *et al.* 2021). In
 119 the present work we do not study the statistical properties of bubble agitation, but it
 120 has to be kept in mind that the self-induced agitation results from wakes interactions,
 121 as already discussed in a homogeneous swarm of confined bubbles where coalescence was
 122 inhibited (Bouche *et al.* 2012, 2014).

123 It is worth pointing out that this flow configuration finds promising applications in
 124 chemical engineering since it is expected to be an alternative reactor of intermediate
 125 size that takes advantage of the confinement to enhance mass transfer, as in monolith
 126 reactors, and of the intense bubble-induced agitation to develop satisfactory in-plane
 127 mixing (Roudet *et al.* 2017; Alméras *et al.* 2018). Some recent applications have been
 128 developed concerning light-activated reactions or cultivation of micro-algae in photo-
 129 reactors that need narrow geometries due to light absorption and attenuation, while

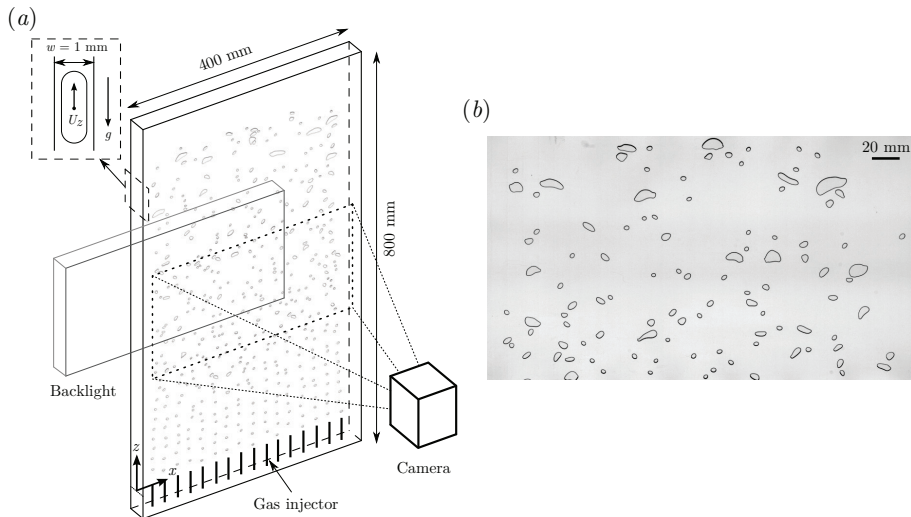


FIGURE 1. (a) Sketch of the experimental facility, showing the field of view of size $358.40 \text{ mm} \times 179.20 \text{ mm}$ for one of the camera recording positions. The zoomed area schematizes the lateral view of the cell with a bubble flattened between the side walls. (b) Example of image taken in one of the three different vertical positions of the camera.

130 keeping efficient mixing and mass transfer requirements (Oelgemoller 2016; Pruvost *et al.*
 131 2017; Thobie *et al.* 2017).

132 The paper is organized as follows. The experimental facility and the techniques devel-
 133 oped to describe the evolution of the population of bubbles are presented in §2. A careful
 134 examination of the performances of the bubble tracking algorithm is also presented in
 135 this section. The statistical properties of the gas flow and their evolution with the bubble
 136 population, for different values of the void fraction at injection, are reported in §3. In
 137 particular, in §3.1 we will introduce a parameter to properly characterize the evolution
 138 of bubble sizes. Then, the results of the rate of change of the population of bubbles and
 139 the measurements of the bubble collision frequency are summarized and discussed in
 140 §3.2. The model associated with the collision frequency is introduced in §4. Finally §5 is
 141 devoted to conclusions.

142 2. Experimental facility and techniques

143 The experimental facility used to characterize the evolution of the bubble size dis-
 144 tribution in a high-Reynolds number confined bubble swarm is presented in §2.1. This
 145 particular flow configuration allowed a direct analysis of the whole bubble population
 146 using shadowgraphy technique, since the planar motion prevented bubble overlap in the
 147 recording plane. In addition to the description of the operating conditions and of the
 148 shadowgraphy technique used, an overview of the image processing algorithm developed
 149 to detect, classify and track the bubbles in the swarm is given in the Appendix §A.

150 2.1. Experimental facility and operating conditions

151 The confined bubble swarm was generated within a quasi-bidimensional vertical cell
 152 filled with distilled water at ambient temperature, being its top section open to atmo-
 153 spheric pressure (Bouche *et al.* 2012, 2014). The cell consists of two parallel glass plates
 154 (800 mm high and 400 mm wide) separated by a thin gap of width $w = 1 \text{ mm}$ (figure 1a).

155 Unlike in previous works related to confined bubble swarms (Bouche *et al.* 2012, 2013,
 156 2014; Alm eras *et al.* 2016, 2018), no electrolyte was added to the liquid so that bubble
 157 coalescence was not inhibited. In addition, the distilled water was regularly renewed to
 158 prevent interface contamination. Air bubbles of uniform size were periodically injected
 159 from the bottom of the cell through an array of 16 capillary tubes of 0.6 mm inner
 160 diameter and 0.8 mm outer diameter (figure 1a). The tubes were equally distributed
 161 along the bottom of the cell and connected to a controlled pressure air feeding chamber.
 162 The pressure drop along the air injection tubes was sufficiently large to ensure a constant
 163 air flow rate along the tubes (Gordillo *et al.* 2007). The bubble detachment frequency,
 164 f_b , was accurately selected firstly setting a certain pressure in the air feeding chamber,
 165 p_g , and, secondly, controlling the air flow rate through each tube using individual valves.
 166 This frequency was checked for each injector using a stroboscopic light before running
 167 each experiment.

168 The volume of the injected bubbles ensured that their sizes were always larger than
 169 the width of the gap, w . Therefore, the bubbles were flattened between the cell walls,
 170 forming a thin liquid film between the bubble interface and the wall (see zoomed area
 171 in figure 1a). In this configuration, independently of the bubble size distribution of the
 172 swarm, no dewetting at the glass plates was observed and the bubbles degrees of freedom
 173 were bounded. The flow above the bubbles goes around sideways, and does not enter the
 174 thin liquid films at rest as in Pavlov *et al.* (2021). Therefore, these thin films are not
 175 expected to play any role in the bubble coalescence processes described in the present
 176 work. Hence, a two-dimensional description of the motion can be adopted as in Roig
 177 *et al.* (2012) and in Filella *et al.* (2015). In that sense, every bubble in the swarm is
 178 described by an equivalent diameter which is defined as $D = (4A_b/\pi)^{1/2}$, being A_b
 179 the projected area of the bubble on the cell plane. The injected gas volume fraction,
 180 $\alpha_0 = \sum_i A_b^i w / (L_x L_z w)$, was determined from the total volume occupied by all the bubbles
 181 in a measuring window a few millimeters above the capillary tubes ($W1$ in figure 2), where
 182 $L_z = 50.83$ mm and $L_x = 328.67$ mm are respectively the height and the width of the
 183 window. In the current experiments, α_0 was varied from 2.4 % to 6.7 % by adjusting
 184 the bubble generation frequency. Table 1 shows the experimental conditions of the four
 185 experimental sets considered in the present work, including the mean equivalent diameter
 186 of the injected bubbles, D_0 . The variations in the sizes of the bubbles generated by
 187 each tube were negligible and a monodispersed bubble swarm was initially formed, as
 188 in Bouche *et al.* (2012, 2014). Additionally, the total air flow rate was estimated as
 189 $Q_g = 4\pi D_0^2 w f_b$, showing a linear increase with α_0 .

190 The bubble swarm at the bottom of the cell is characterized by α_0 and by the
 191 non-dimensional parameters governing the motion of an isolated bubble of equivalent
 192 diameter at injection, D_0 . These include the Archimedes number, $Ar_0 = \sqrt{gD_0} D_0/\nu$,
 193 the confinement ratio, $\delta_0 = w/D_0$, and the Bond number $Bo_0 = \rho g D_0^2/\sigma$, where g is the
 194 gravity, ν and ρ the liquid kinematic viscosity and density, w the thickness of the cell
 195 and σ the surface tension. Under the conditions reported here, these parameters lie in
 196 the following ranges: $630 \leq Ar_0 \leq 850$, $0.24 \leq \delta_0 \leq 0.29$, and $1.79 \leq Bo_0 \leq 2.11$. For
 197 confined bubbles of equivalent diameter $D \geq D_0$, the mean rise velocity of an isolated
 198 bubble can be estimated by (Filella *et al.* 2015)

$$U_b \simeq 0.75(w/D)^{1/6} \sqrt{gD}, \quad (2.1)$$

199 which in dimensionless form can be expressed as,

$$Re \simeq 0.75 \delta^{1/6} Ar, \quad (2.2)$$

200 where $Re = U_b D/\nu$ and $Ar = \sqrt{gD} D/\nu$ are the Reynolds and Archimedes number of

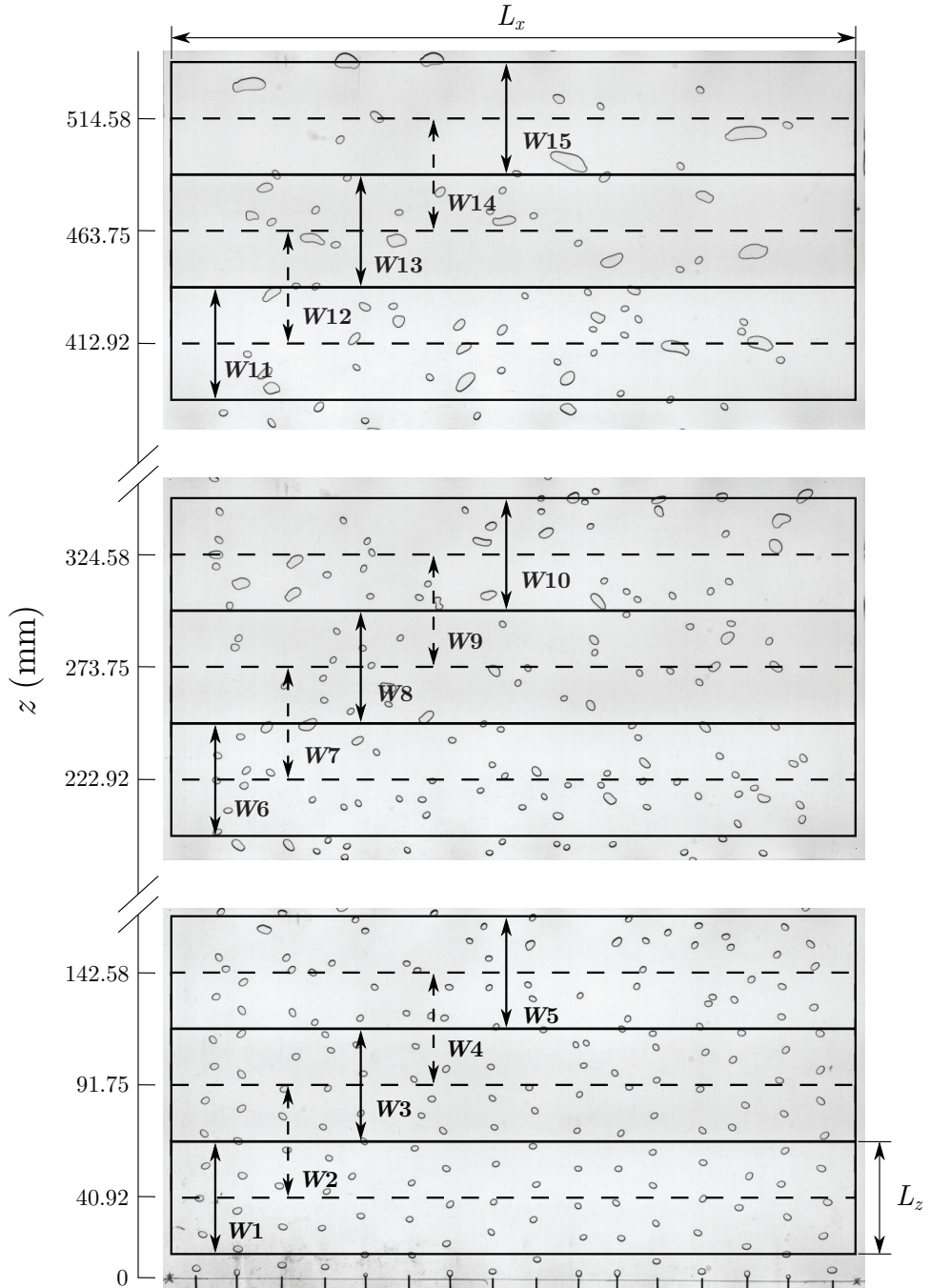


FIGURE 2. General view of the three recording positions for $\alpha_0 = 3.2\%$. The 15 measuring windows used for the spatial discretization are superimposed on the images. The height of each measuring window is $L_z = 50.83$ mm while its width almost comprises the whole transverse spanwise of the cell, $L_x = 328.67$ mm. The vertical axis denotes the position of the middle point of some of the measuring windows.

	α_0 (%)	D_0 (mm)	p_g (bar)	f_b (s ⁻¹)	Q_g (m ³ s ⁻¹) × 10 ⁶
Set 1	2.4	3.65 ± 0.20	0.6	7	1.18 ± 0.13
Set 2	3.2	3.68 ± 0.22	0.7	9	1.53 ± 0.19
Set 3	4.9	3.85 ± 0.28	0.8	13.5	2.51 ± 0.38
Set 4	6.7	3.96 ± 0.23	0.9	18	3.54 ± 0.42

TABLE 1. Injection conditions of the four experimental sets considered in the present work: α_0 , gas volume fraction at the bottom of the cell; D_0 , mean equivalent diameter of the bubbles injected; p_g , pressure at the air feeding chamber; f_b , bubble generation frequency; Q_g , air flow rate.

201 a bubble of size D . The bubble Reynolds number, $Re_0 = U_b D_0 / \nu$, can then be defined,
202 and ranges here from 380 to 500. The gap Reynolds number, $Re_0 \delta_0^2$ can then also
203 be introduced to assess the inertial regime, as it varies between 28 and 32. Thus, the
204 flow can be considered to be dominated by inertia (Bush & Eames 1998) for all bubble
205 sizes involved in the swarm. Bubbles at injection initially behave as isolated bubbles
206 exhibiting oscillatory paths coupled to their unsteady wakes that generate periodic vortex
207 shedding. Their in-plane projected shape is deformed and can be considered as an ellipse
208 of moderate eccentricity (Roig *et al.* 2012; Filella *et al.* 2015). For further discussion,
209 general ideas can be retained. First, the velocity disturbances induced by bubbles in the
210 liquid are mainly parallel to the plates, except in the close vicinity of the bubbles. Then,
211 the order of magnitude of the liquid velocity in the bubble's wake is \sqrt{gD} . The wake is
212 nevertheless strongly attenuated by shear stress at the walls within a characteristic time
213 scale proportional to the viscous one, $\tau_\nu = w^2 / (4\nu)$. Therefore, in the swarm the agitation
214 in the liquid results from direct interactions of localized random flow disturbances of
215 various sizes as in the homogeneous swarm studied by Bouche *et al.* (2014).

216 The swarm of bubbles generated was recorded using shadowgraphy in a measurement
217 region that spanned almost the entire horizontal width of the cell (figure 1). To that
218 aim, the cell was illuminated from behind with an uniform, constant and diffused white
219 light perpendicular to the cell plane (figure 1a). Placing the light source at one side
220 of the cell, a camera (Photron APX) equipped with a 85 mm lens was used to take
221 images of 2¹⁰ levels of gray and of size 1024 × 512 pixels, with an exposure time of
222 1/2000 s, from the other side. In order to analyze the evolution of the population of
223 bubbles as they rise, while maintaining the desired resolution, the backlight and the
224 camera were placed at three different positions (figure 2). Transverse homogeneity of
225 the flow was observed. Therefore, the downstream evolution of the bubble swarm was
226 described by a statistical analysis of the bubble population characteristic parameters
227 averaged over the horizontal width of the cell. In order to avoid possible errors due to
228 border effects, the analysis was performed in a recording region, placed in the middle
229 of each image, which consisted of a rectangle of size 328.67 mm × 152.49 mm with a
230 pixel-size resolution of 350 μm (figure 1b). Moreover, to increase the spatial resolution
231 of the measurements, the recording region was divided into five windows of horizontal
232 length $L_x = 328.67$ mm and vertical length $L_z = 50.83$ mm, with 50 % of overlapping, as
233 indicated in figure 2. Two types of measurements were performed, depending on the image

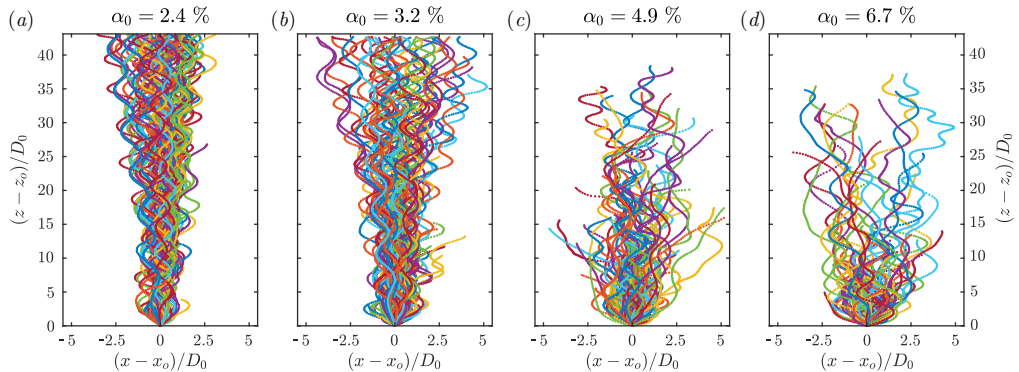


FIGURE 3. Superimposed trajectories of 100 bubbles detected in the field of view of the first recording position, $z < 160$ mm, for the different injection conditions (a) $\alpha_0 = 2.4$ %; (b) $\alpha_0 = 3.2$ %; (c) $\alpha_0 = 4.9$ % and (d) $\alpha_0 = 6.7$ %. Each trajectory is defined as a succession of points corresponding to the bubble centroid at each instant. The origin (x_o, z_o) is defined as the position where the bubble is first detected. The positions are normalized using the corresponding injection diameter D_0 .

234 acquisition frequency. First, a series of experiments taking video images of the swarm
 235 at 250 fps were conducted. This recording rate was high enough to track the bubbles as
 236 they rose along the field of view. Thus, bubble collisions could be detected and tracked
 237 to determine whether the colliding bubbles coalesced, generating new larger bubbles, or
 238 eventually separated, which allowed us to determine the bubble collision frequency, h , as
 239 well as the efficiency, λ . Measurements also allowed us to detect breakup events, giving
 240 *birth* to smaller daughter bubbles, although this phenomenon was rare in this study. For
 241 this analysis, high-speed movies of 25 s duration were recorded at the three positions.
 242 The total duration of the recordings included between 20 000 and 75 000 bubble records
 243 per position, depending on the injection conditions and on the measuring location. In
 244 addition to the experiments recorded at high frequency, at each recording position, sets of
 245 around 3 000 uncorrelated images were recorded at a frame rate of 1/2 fps to ensure that
 246 the bubbles in one image were not recorded in the following one. Thus, the total number
 247 of bubbles detected at each position varied between 25 000 and 250 000, depending on
 248 the injected air flow rate and on the recording position. This ensured a statistically
 249 converged and unbiased measurement of parameters of the bubble population that can
 250 be obtained from low frequency experiments such as the volume probability density
 251 function. Satisfactory comparison of the information that could be obtained from both
 252 types of measurements indicated that the statistical parameters extracted only from the
 253 high-frequency records were indeed robust and meaningful.

254 Details of the digital image processing methods specifically developed in this work to
 255 detect and classify the bubbles in the swarm are given in §A.1. In addition, the techniques
 256 designed to track the bubbles and detect the collisions, as well as the coalescence and
 257 breakup events are described in §A.2. Additional information can be found in Ruiz-Rus
 258 (2019).

259 2.2. Performance of the bubble tracking algorithm (BTA)

260 The results obtained with the bubble tracking algorithm described in the Appendix
 261 §A, consist of the record of the bubbles along the field of view for each position. The
 262 information stored for each bubble includes the projected area (bubble volume), the
 263 centroid location, the bubble velocity components, as well as the bubble lifespan and

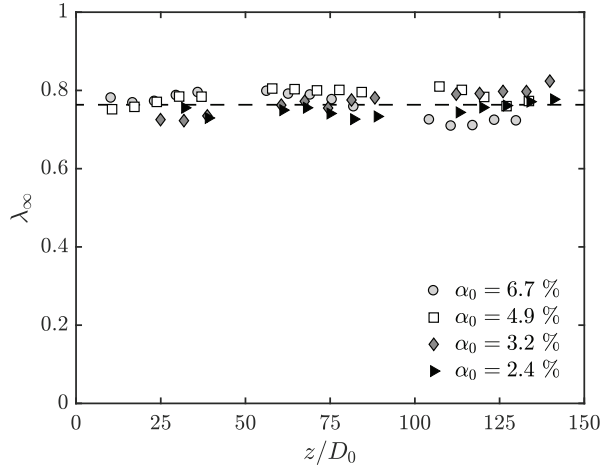


FIGURE 4. Mean collision efficiency of the populations of bubbles, defined as the fraction of collisions that ends up in coalescence, versus the downstream distance normalized by the corresponding injection diameter D_0 . The figure shows that λ_∞ remains constant and does not depend on α_0 .

264 the types of birth and death events. In addition, family trees are established for each
 265 newly generated bubble, including the parents in a birth from coalescence, or the mother
 266 and the sibling in a birth from breakage. The performance of the BTA algorithm can be
 267 estimated, first, from the fact that more than 99% of the detected bubbles can be tracked,
 268 the remaining ones being associated to specific events with simultaneous coalescence and
 269 breakup in agglomerates of bubbles.

270 As an example, figure 3 shows a set of bubble trajectories for each injection condition
 271 at the first recording position. In this figure, regardless of where the bubble trajectories
 272 begin, they have been displaced to the same origin, with x_o and z_o being the initial
 273 positions of the bubbles. It can be observed that the horizontal dispersion of the bubbles
 274 increases with the injected air volume fraction and with the vertical position, showing
 275 the effects of the liquid velocities induced by the wakes of the population of bubbles.
 276 The bubble lifespan is typically larger for the lowest values of α_0 (figure 3a, b), since the
 277 number of coalescence events is still low at this recording position. The trajectories show
 278 the characteristic path oscillations described by Roig *et al.* (2012) for isolated bubbles,
 279 indicating the weak effect of the hydrodynamic interactions at these low void fractions.
 280 However, the degree of coalescence substantially increases with α_0 , resulting in much
 281 shorter trajectories (figure 3c, d).

282 The first quantitative measurement extracted from the BTA is the collision efficiency.
 283 It represents the ratio between the number of coalescence and that of collisions. As
 284 mentioned before, the confinement of the bubbles imposed in this configuration highly
 285 increases the efficiency of the collisions. The mean collision efficiency, λ_∞ , obtained
 286 considering all the collisions detected at each measuring window, is plotted in figure 4 for
 287 the four values of α_0 tested in this work. Our results indicate that the collision efficiency
 288 barely depends on the size of the colliding bubbles. In fact, considering the collision
 289 efficiency of different pairs of bubbles, differences lower than 5% were found with respect
 290 to λ_∞ . In addition to being a very high efficiency, it should be noted that λ_∞ does not
 291 vary with the concentration of bubbles, nor with z . In fact, the figure shows that its value
 292 can be considered constant and approximately equal to 80%.

293 Moreover, the tracking method allows a direct analysis of the coalescence events. In that

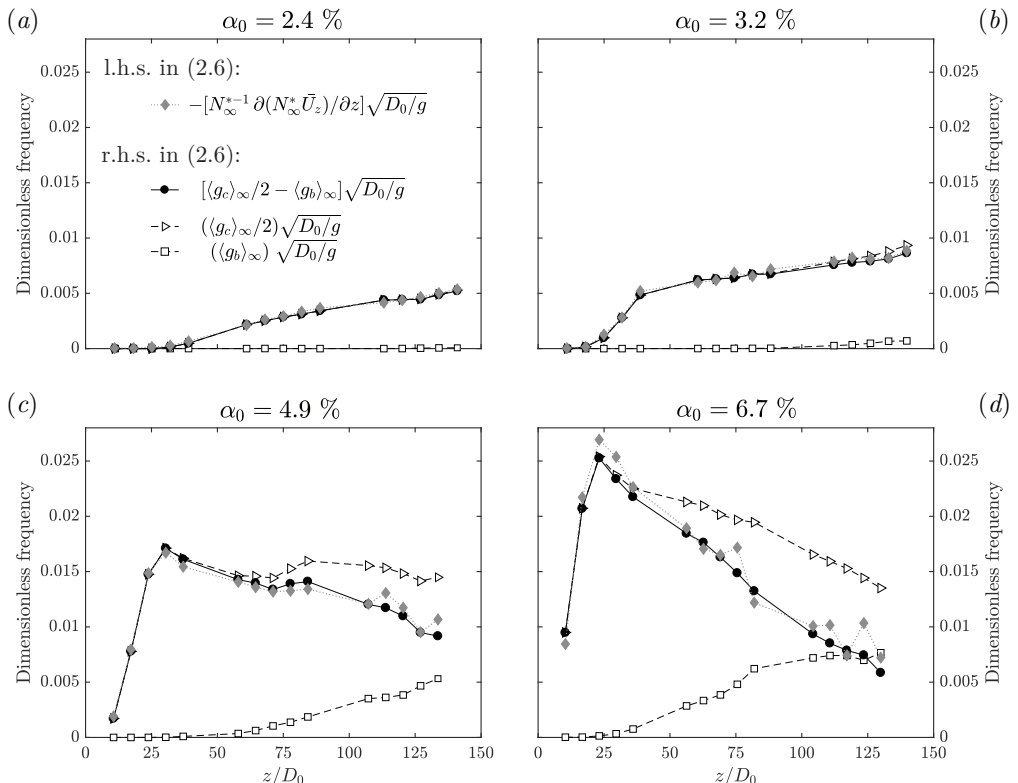


FIGURE 5. Downstream evolution of the different rates of change of the whole population of bubbles for different injection conditions, (a) $\alpha_0 = 2.4\%$; (b) $\alpha_0 = 3.2\%$; (c) $\alpha_0 = 4.9\%$ and (d) $\alpha_0 = 6.7\%$. All these frequency terms have been made dimensionless with $\sqrt{g/D_0}$. Both sides of the averaged PBE, as expressed in (2.6), are shown with solid symbols, l.h.s. (diamonds) and r.h.s. (circles). In addition, the different rate of change terms in the r.h.s. of (2.6) are represented with open symbols, half of the mean coalescence frequency (triangles) and the mean breakup frequency (squares).

294 sense, any detected collision is individually tracked (see §A.2), obtaining the position at
 295 which it initially occurs as well as the corresponding information for the colliding bubbles.
 296 In addition, the BTA can be used to obtain the number of bubbles of volume v that die
 297 due to coalescence, and the mean coalescence frequency of all bubbles at each position,

$$\langle g_c \rangle_\infty = \frac{\int_0^\infty n(v)g_c(v)dv}{\int_0^\infty n(v)dv}, \quad (2.3)$$

298 that represents the frequency at which a bubble of any size coalesces with other bubbles.
 299 In the experiments performed in this work, most of the daughter bubbles which are
 300 born due to coalescence come from previous binary collisions. Thus, since the total
 301 number of collisions which end up in coalescence, γ_∞ , during the measuring time, T , in a
 302 population of N_∞ bubbles, is half of the bubbles dying due to coalescence, $N_\infty \langle g_c \rangle_\infty / 2$,
 303 the mean bubble coalescence frequency can be directly obtained from the experimental
 304 measurements as

$$\langle g_c \rangle_\infty = \frac{2\gamma_\infty}{N_\infty T}. \quad (2.4)$$

305 Similar to the mean coalescence frequency, $\langle g_c \rangle_\infty$, the mean breakup frequency of bubbles

at each position, given by $\langle g_b \rangle_\infty = \int_0^\infty n(v)g_b(v)dv / \int_0^\infty n(v)dv$, can be directly obtained as

$$\langle g_b \rangle_\infty = \frac{\psi_\infty}{N_\infty T}, \quad (2.5)$$

where ψ_∞ is the number of breakup events observed during the time T .

Thus, the accuracy and convergence of the tracking analysis of the experiments performed at high rates of acquisition, can be checked by comparing both sides of the equation (1.2) averaged over all bubble sizes, assuming that both coalescence and breakup are binary processes. To that aim, the l.h.s. in the averaged PBE can be achieved by integration of equation (1.2) over the whole range of bubbles (Friedlander 1977). Thus, applying the Leibnitz rule for integration and substituting (1.5) and (1.6) into (1.2), in the one-dimensional, steady state situation of interest here, the averaged PBE simplifies to (Kocamustafaogullari & Ishii 1995; Soligo *et al.* 2019)

$$-\frac{1}{N_\infty} \frac{\partial (N_\infty \bar{U}_z)}{\partial z} = \frac{\langle g_c \rangle_\infty}{2} - \langle g_b \rangle_\infty, \quad (2.6)$$

where \bar{U}_z is the mean rising velocity of the bubbles in the measuring window. Figure 5 shows the different terms in both sides of equation (2.6), evaluated at various measuring locations, for all the experimental injection conditions. In that case, the frequency terms have been made dimensionless making use of $\sqrt{g/D_0}$, while the downstream locations are normalized with the injection diameter D_0 , corresponding to each experimental injection condition. As expected, a fairly good agreement is observed between both sides of the equation (black circles and gray diamonds, respectively). This result confirms the validity of the experimental procedure, as well as the effectiveness of the bubble tracking method and the convergence of the results obtained. In addition, it can be noticed that some breakup events (hollow squares) also take place in the swarm, especially for the higher values of α_0 (figure 5c, d).

3. Description and discussion of bubble coalescence in the evolving swarm

An overview of the results obtained by the BTA has shown that the evolution of the population of bubbles is mainly governed by bubble coalescence, with a weak contribution of bubble breakup in some cases (figure 5). These processes, that lead to variations in the bubble size distribution, are driven by the liquid agitation in the swarm, which in turn is induced by the interaction of the wakes of bubbles of different sizes that constitute the swarm. Consequently, it is necessary to characterize the different stages of the evolution of the bubble population to adequately elucidate the mechanisms that govern the coalescence process.

3.1. Spatial evolution of the bubble population

In the present configuration there is no external liquid flow that carries the bubbles and they rise due to buoyancy effects. The downstream evolution of the population of bubbles can be described in terms of the flux of bubbles crossing each z position. An estimation of the averaged flux is given by the local net number of bubbles detected in each measuring window, N_∞^* , multiplied by their corresponding mean velocity, \bar{U}_z , obtained by the BTA. Figure 6(a) shows the downstream evolution of the bubbles flux for each injection condition. The fact that the flux of bubbles decreases with the dimensionless downstream location z/D_0 , indicates that coalescence leads the evolution

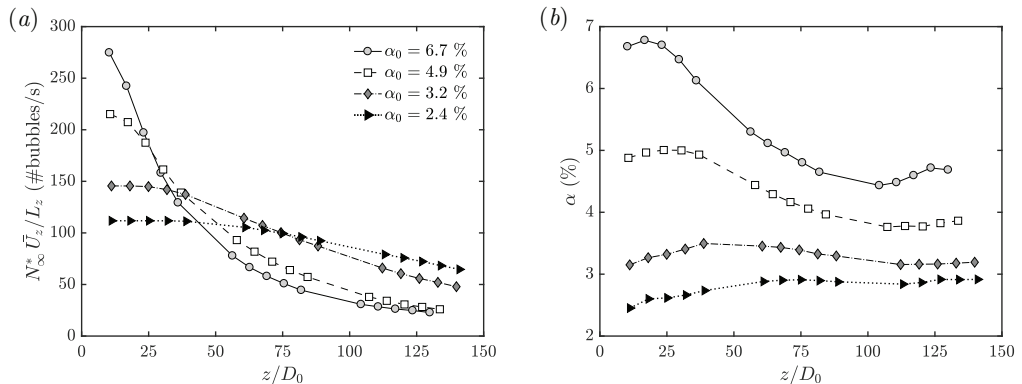


FIGURE 6. (a) Downstream evolution of the total flux of bubbles measured in each position (window) for the different experimental injection conditions. (b) Downstream evolution of the local gas volume fraction, obtained from the total volume occupied by all the bubbles present in each window. The downstream locations have been normalized by the corresponding injection diameter D_0 .

of the distribution of bubbles, even in the cases where there are some breakup events, as previously shown in figure 5. The rate of change of the population depends on the initial number of bubbles, $N_{\infty}^*(0)$, which is directly related to the selected bubble generation frequency, f_b , and thus, to the injected air volume fraction, α_0 . For high void fractions (i.e. $\alpha_0 = 4.9$ and 6.7 %, respectively), near the bottom of the cell, the amount of bubbles of injection size D_0 quickly decreases as the bubbles rise. In fact, strong bubble-bubble interactions occur in the regions close to the injectors, giving rise to collisions and coalescence events. Once the bubbles start coalescing, larger bubbles are generated leading to a coalescence cascade which rapidly involve pairs of bubbles of wider ranges of sizes. As z/D_0 increases the flux decreases less rapidly. In fact, the reduction in the total number of bubbles composing the population causes the net amount of coalescence events to decrease too. Although the rate of change of the bubbles flux decreases with the downstream distance, there is no evidence of reaching a final frozen-state where coalescence would become negligible. It has to be pointed out that at higher positions of the cell, as previously noticed in figure 5(c,d), bubble breakup occurs, competing with coalescence. The unstable nature of the largest bubbles generated in these cases as well as the interaction with stronger bubble-induced liquid velocities, increases the relevance of breakage far from the injection point. On the other hand, for lower void fractions (i.e. $\alpha_0 = 2.4$ % and 3.2 %), figure 6(a) shows that the bubbles take longer to begin to coalesce. In these cases, the bubble flux initially remains constant up to a certain position where it starts to decay at a rate that decreases as α_0 decreases. This is related with the lower amount of bubbles generated under these conditions and the larger distances between bubbles at the initial positions. However, as they rise, the injected bubbles lose memory of the injection conditions and begin to adopt the oscillatory motion which characterizes these ellipsoidal bubbles within the confined cell (Roig *et al.* 2012; Filella *et al.* 2015). At a given height that depends on the generation frequency (Sanada *et al.* 2005), the trajectories of the bubbles scatter under the effect of the perturbations in the liquid, giving rise to bubble-bubble interactions and to the subsequent collisions and coalescence events (see *W4* and *W5* in figure 2).

Figure 6(b) shows, for each injection condition, the downstream evolution of the local air volume fraction $\alpha(z)$, defined as the volume occupied by the entire population of bubbles present at each measuring window, divided by the volume of the window. At

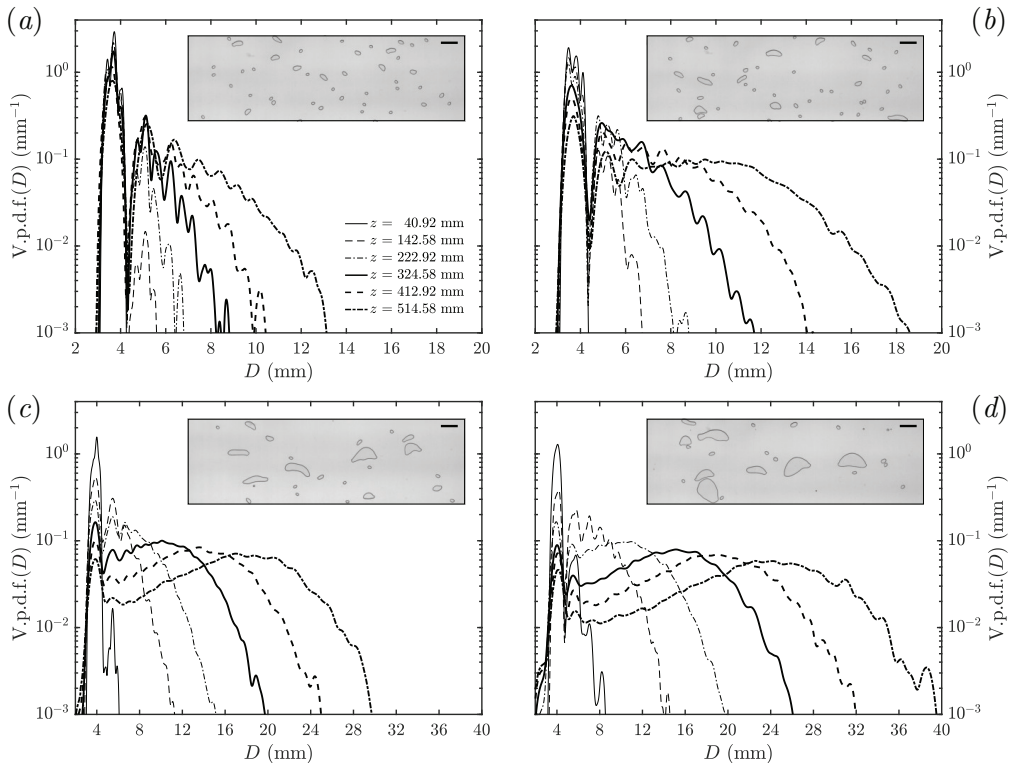


FIGURE 7. Downstream development of the bubble size distribution described by the volume-size bubble p.d.f. for (a) $\alpha_0 = 2.4\%$, (b) $\alpha_0 = 3.2\%$, (c) $\alpha_0 = 4.9\%$ and (d) $\alpha_0 = 6.7\%$. Only some measuring locations have been plotted for clarity. The image inside each panel corresponds to a cell height around $z = 412.92$ mm. The scale bar indicates a length of 20 mm.

379 variance with homogeneous monodispersed bubble swarms where the gas volume fraction
 380 remains constant under constant injection conditions (Martinez Mercado *et al.* 2010;
 381 Bouche *et al.* 2012; Colombet *et al.* 2015), in the present swarm, $\alpha(z)$ also varies with
 382 z/D_0 , due to the evolution of the distribution of sizes and to the fact that the velocity
 383 of the bubbles varies with their sizes. Indeed, the absence of an external liquid flow
 384 implies that the mean rising velocity of the gas phase is mainly imposed by the buoyancy
 385 exerted on the different bubble sizes coupled to the underlying fluid motion generated
 386 by hydrodynamic interactions. Therefore, the local volume fraction $\alpha(z)$ is affected not
 387 only by the injected air flow-rate, but also by the evolution of the distribution of bubbles
 388 that induces buoyancy-driven variations on the mean rising velocity of the gas phase.

389 In order to determine the distribution of bubble sizes at each measuring window, the
 390 equivalent diameters of the bubbles were obtained from image processing (see §A.1) to
 391 compute the bubble volume probability density function (Martínez-Bazán *et al.* 1999a),

$$\text{V.p.d.f.}(D) = \frac{w D^2 \text{ p.d.f.}(D)}{\int_{D_{min}}^{D_{max}} w D^2 \text{ p.d.f.}(D) dD}, \quad (3.1)$$

392 which represents the volume occupied by bubbles of size D compared to that of the
 393 entire distribution. In equation (3.1) D_{min} is the smallest bubble size of the distribution
 394 and D_{max} the largest one. The downstream evolution of the V.p.d.f. resulting from

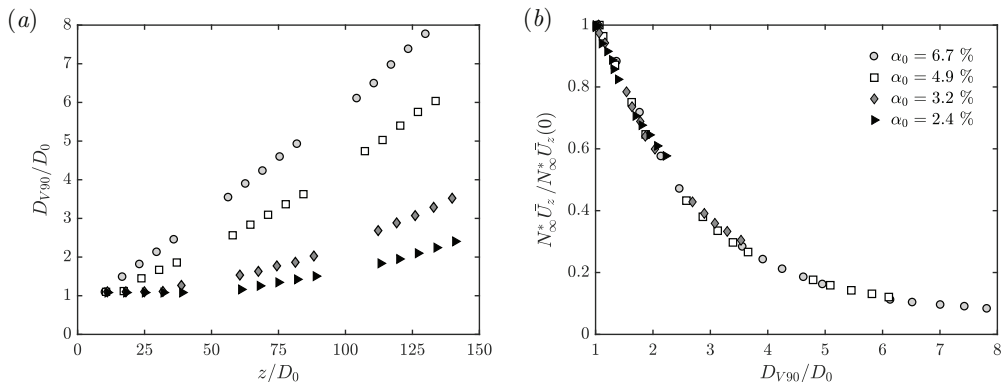


FIGURE 8. (a) Evolution of D_{V90} with the downstream location, both normalized with the corresponding bubble injection diameter D_0 , for the different injection conditions. Notice that, D_{V90}/D_0 remains unchanged until the coalescence process starts, leading to larger bubbles. (b) Evolution of the flux of bubbles normalized with that at the first measuring window, $N_{\infty}^* \bar{U}_z(0)$, as a function of D_{V90}/D_0 .

395 coalescence, and eventually breakup, is shown in figure 7 for the four experimental
 396 conditions reported in Table 1. For the sake of clarity, we have only plotted six measuring
 397 locations. Qualitatively, similar downstream evolutions are observed for the four cases:
 398 the nearly monodispersed distribution of bubbles observed close to the bottom of the
 399 cell progressively widens further downstream due to bubble coalescence. Since bubbles
 400 of constant size, D_0 , are periodically injected at the bottom of the cell, for low values
 401 of α_0 , the initial V.p.d.f. is a narrow distribution around D_0 (see the distribution at
 402 $z = 40.92$ mm in figures 7a and b). In fact, in these cases, coalescence is not observed
 403 until $z = 142.58$ mm (figure 7a,b), as previously noted from the evolution of the total flux
 404 of bubbles shown in figure 6(a). However, for larger values of α_0 , at the first measuring
 405 window, a secondary peak is already observed at $D \simeq \sqrt{2}D_0$, indicating the existence
 406 of some coalescence events of bubbles of size D_0 ($z = 40.92$ mm in figure 7c,d). It is
 407 worth noticing the existence of additional peaks at $\sqrt{3}D_0, \sqrt{4}D_0, \dots$, corresponding to
 408 added volumes of the injection bubbles resulting from successive coalescence events (Néel
 409 & Deike 2021). Nevertheless, as the coalescence process evolves, such peaks (associated
 410 with classes of finite extension) attenuate, generating broader and smoother distributions
 411 far from the injection point. The V.p.d.f.s exhibit large tails as the coalescence cascade
 412 progresses. In fact, it can be observed that the size of the largest bubbles found at a certain
 413 distance increases with α_0 . This fact is clearly illustrated in the images displayed as insets
 414 in figure 7, which show characteristic snapshots of the swarm for each experimental
 415 condition at $z = 412.92$ mm.

416 For all values of α_0 , despite the differences in the downstream evolution of the rate
 417 of change of the number of bubbles, similar shapes of the distribution are found at
 418 different positions, which can be understood as equivalent stages of the coalescence
 419 cascade process. For example, the distribution at $z = 324.58$ mm in figure 7(a) is similar
 420 to that at $z = 222.92$ mm in figure 7(b), the distribution at $z = 324.58$ mm in figure 7(b)
 421 matches that at $z = 142.58$ mm in figure 7(c) and the distribution at $z = 514.58$
 422 mm in figure 7(c) resembles that at $z = 412.92$ mm in figure 7(d). The similarity in
 423 the distribution evolutions reveals that the various swarms considered follow the same
 424 coalescence cascade, independently of the value of α_0 . However, the rate of change of the
 425 swarm strongly depends on the void fraction, which is directly related to the amount of

bubbles forming the population, as can be inferred from equation (1.5). It will take longer for low values of α_0 (figure 7*a,b*) than for larger ones (figure 7*c,d*) to reach a given stage of the distribution of sizes (i.e. a given shape), although each size will undergo the same coalescence cascade independently of α_0 . Taking this into account, the evolution of the bubble size distribution is characterized by a diameter representative of the population of bubbles. For this purpose, we used the statistically robust parameter, D_{V90} (Hinze 1955; Martínez-Bazán *et al.* 1999*b*), defined as the diameter of a bubble such that 90% of the total volume of the population of bubbles is contained within bubbles smaller than D_{V90} . This characteristic diameter represents the size of the largest bubbles in the distribution which, as they rise, will induce the largest velocity fluctuations in the liquid.

Figure 8(*a*) shows the downstream evolution of D_{V90} for the four injection conditions, reflecting the increase of its rate of change with α_0 . Notice that, for $\alpha_0 = 2.4\%$ and 3.2% , D_{V90} barely changes for $z < 150$ mm, indicating that coalescence does not start in those cases until $z > 150$ mm. However, for $\alpha_0 = 4.9\%$ and 6.7% coalescence is already observed near the injection position. In addition, figure 8(*b*) shows the evolution of the flux of bubbles normalized by that of the first measuring window, $N_\infty^* \bar{U}_z(0)$, as a function of the characteristic diameter D_{V90} normalized by the diameter of the injected bubbles, D_0 . It can be observed that the four plots collapse on the same curve, corroborating that the population of bubbles follow similar coalescence cascade processes and that D_{V90} is the proper variable to describe the evolution of the population of bubbles of the different swarms. In that sense, D_{V90}/D_0 , can be seen as a variable similar to the dimensionless time, t/τ , proposed by Smoluchowski (1917) to describe the Brownian coagulation of particles within nearly monodispersed systems (see Chandrasekhar 1943; Friedlander 1977, for reports of this work in English), being τ the characteristic coagulation or decay time, usually called *half-life* of the population. So, in the following, D_{V90} will be considered as the characteristic parameter to determine the evolution of the swarm. This will allow us to consider the coalescence frequency as an unknown that varies with the self-induced evolution of the population, which includes the influence of the *a priori* unknown velocities of each size, as well as the α_0 dependence.

As already indicated above, the aim of the present work is to experimentally determine the coalescence frequency of a pair of bubbles of sizes D and D' respectively in the bubble swarm. To be able to do it, large enough size ranges have to be defined to ensure that the number of bubbles included in each range is sufficiently high to have enough number of colliding bubbles, and thus obtain statistically converged results. For this purpose, we discretized the population of bubbles obtained from the experiments in different size classes, denoted as class 0, 1, 2 and so on. Every class is represented by a diameter D_k and includes bubble sizes in the range $D_k - \Delta_k/2 \leq D \leq D_k + \Delta_k/2$, within a size bin of width Δ_k . The diameter D_k represents the middle size of the bin and corresponds to integer values of the injection bubble volume, accounting for volume-conservative coalescence events. Thus, the initial class corresponds to the injection bubbles, D_0 . The following class is associated to the coalescence of two bubbles of size D_0 , being $D_1^2 = 2D_0^2$. The rest of the classes, D_k , are defined as the diameter of the bubble formed from the coalescence of two bubbles belonging to the two preceding classes, $D_k^2 = D_{k-1}^2 + D_{k-2}^2$. Therefore, the different classes represent added volumes of the injection bubbles resulting in the following diameters: $D_1 = \sqrt{2}D_0$, $D_2 = \sqrt{3}D_0$, $D_3 = \sqrt{5}D_0$, $D_4 = \sqrt{8}D_0$, $D_5 = \sqrt{13}D_0$, $D_6 = \sqrt{21}D_0$, $D_7 = \sqrt{34}D_0$ and $D_8 = \sqrt{55}D_0$. The different sizes of the bins, Δ_k , were chosen looking for substantial but smooth variations of the bubble characteristics. Such definition of bubble classes and their corresponding limits allowed us to have an amount of bubbles sufficiently large in each class to observe enough collisions events among bubbles of different classes, ensuring a good statistical convergence of the data.

α_0 (%)		Set 1	Set 2	Set 3	Set 4
		2.4	3.2	4.9	6.7
k		$D_k \pm \Delta_k / 2$ (mm)			
0	(○)	3.65 ± 0.27	3.68 ± 0.27	3.85 ± 0.32	3.96 ± 0.32
1	(▶)	5.16 ± 0.37	5.20 ± 0.38	5.45 ± 0.43	5.60 ± 0.44
2	(☆)	6.32 ± 0.78	6.37 ± 0.78	6.67 ± 0.78	6.86 ± 0.81
3	(■)	8.16 ± 1.06	8.23 ± 1.08	8.62 ± 1.10	8.85 ± 1.18
4	(◁)	-	10.40 ± 1.10	10.90 ± 1.20	11.20 ± 1.20
5	(▼)	-	13.26 ± 1.77	13.90 ± 1.80	14.27 ± 1.87
6	(◇)	-	-	17.67 ± 2.00	18.14 ± 2.10
7	(★)	-	-	22.48 ± 2.81	23.08 ± 2.85
8	(△)	-	-	-	29.36 ± 3.43

TABLE 2. Description of the bubble size classes defined for each experimental set. Here, k denotes the bubble class indicating the symbols used to represent them, D_k is the mean diameter describing the class and Δ_k the width of the size bin containing the class.

476 Details of the bubble classes defined for the different injection conditions are listed in
477 Table 2.

478 Considering the bubble classes defined in Table 2, the number of bubbles of a certain
479 class per unit volume, N_k , is obtained integrating equation (1.3) between the size limits
480 of the corresponding bin, $D_k - \Delta_k / 2$ and $D_k + \Delta_k / 2$. The evolution of the fraction of
481 bubbles of each class, N_k / N_∞ , is represented in figure 9, as a function of D_{V90} / D_0 for
482 $\alpha_0 = 6.7\%$, showing the contribution of the amount of bubbles of each class to the whole
483 population in every stage of the coalescence process. Note that, as shown in the inset of
484 figure 9, the fraction of injection bubbles (class $k = 0$) is always larger than those of the
485 other classes, indicating that there is still a considerable amount of bubbles of size D_0
486 remaining even far from the injection point. This fact reveals the appreciable presence
487 of these small bubbles even at stages in which the coalescence cascade has accounted
488 nearly 8^2 events. After a rapid decrease during the early stages of the evolution, the
489 fraction of injection bubbles almost stabilizes around half of the total number of bubbles.
490 However, the evolution of the fraction of all the other classes remarkably differs from
491 that of the initial bubbles. In fact, a certain class of bubbles does not begin to form
492 until a pair of smaller bubbles, whose sum of volumes is equal to the volume of the
493 forming bubble, coalesce. First, the number of bubbles of classes $k > 0$ increases due
494 to coalescence of smaller bubbles. Afterwards, when the number of bubbles of a given
495 class becomes sufficiently large, they start to coalesce forming larger bubbles. Eventually,
496 when the number of coalescing bubbles of a class k is larger than the number of bubbles
497 that are generated from the coalescence of smaller ones, N_k / N_∞ decreases. Indeed, the
498 evolution of the concentration of a certain bubble class within the swarm is driven by
499 the balance between the coalescence rate of smaller bubbles that form bubbles of this
500 class, and their rate of coalescence with all the others, as is clearly established by equation
501 (1.5). The coalescence rate in the balance equation (1.8) are determined from the collision

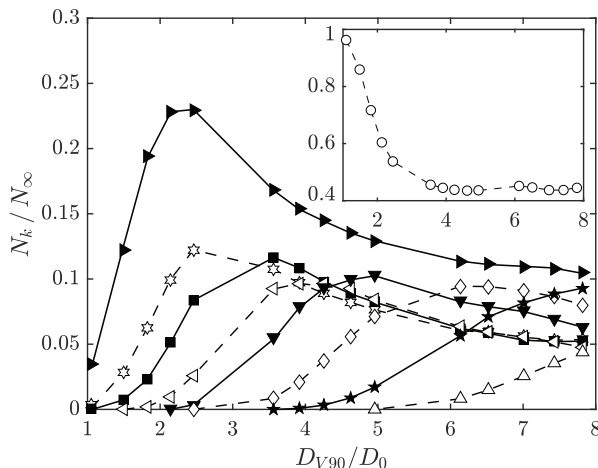


FIGURE 9. Evolution of the fraction of bubbles of each class with D_{V90}/D_0 for $\alpha_0 = 6.7\%$. Similar values are obtained for the other injection conditions. The fraction of bubbles belonging to the injection class is displayed in the inset for clarity. The symbols represent the different bubble classes according to Table 2.

502 frequencies of pairs of bubbles, $h(D_k, D_{k'})$, whose experimental values will be obtained
 503 in §3.2 and modelled in §4.

504 3.2. Determination and analysis of the bubble pair collision frequency, $h(D_k, D_{k'})$

505 Considering the discretization in bubble classes given in Table 2, the number of bubbles
 506 per unit volume of a given class k that *die* per unit time due to coalescence represents
 507 the *coalescence death rate*, commonly expressed as

$$\dot{D}_{ec}(D_k) = - \int_0^\infty \lambda(D_k, D_{k'}) h(D_k, D_{k'}) n(D_k) n(D_{k'}) dD_{k'} = -g_c(D_k) n(D_k). \quad (3.2)$$

508 In equation (3.2), $h(D_k, D_{k'})$ is the collision frequency of bubbles of class D_k with bubbles
 509 of size $D_{k'}$ and has units of $m^3 s^{-1}$, and $n(D_k)$ is the number density of bubbles with
 510 units of m^{-3} , thus $\dot{D}_{ec}(D_k)$ has units of $m^{-3} s^{-1}$. Note that, since $\lambda(D_k, D_{k'}) = \lambda_\infty$ is
 511 constant in the present case, $h(D_k, D_{k'})$ can be treated indistinctly as the collision or
 512 the coalescence frequency of the pair of bubbles. Having this in mind, $h(D_k, D_{k'})$ was
 513 obtained from the experiments performed at high acquisition rates, applying the bubble
 514 tracking and coalescence detection algorithm described in the Appendix §A, as

$$h(D_k, D_{k'}) = \frac{\Gamma_{kk'}}{N_k N_{k'}}. \quad (3.3)$$

515 In equation (3.3), $\Gamma_{kk'}$ is the number of bubbles of class k colliding with bubbles of class
 516 k' in the measuring window, of volume $L_z \times L_x \times w$ (see figure 2), per unit time, and
 517 N_k and $N_{k'}$ are respectively the number of bubbles of class k and k' accounted in the
 518 volume of the measuring window. Thus, the rate of loss of bubbles of class k , $\dot{D}_{ec}(D_k)$,
 519 corresponds to the frequency at which effective collisions of bubbles of size D_k with the
 520 rest of the bubbles take place, which, assuming that $\lambda(D_k, D_{k'}) = \lambda_\infty$ is constant (see
 521 figure 4), reduces to $\dot{D}_{ec}(D_k) = \lambda_\infty \sum_{k'=0}^\infty \Gamma_{kk'}$. Notice that, considering all the bubbles
 522 of the distribution which collide per unit time, $\Gamma_\infty = \sum_{k=0}^\infty \sum_{k'=0}^\infty \Gamma_{kk'}$, the total number
 523 of coalescence events in expression (2.4), can also be obtained as $\gamma_\infty/T = \lambda_\infty \Gamma_\infty/2$. It
 524 is worth indicating that the models for h have been commonly derived by making an

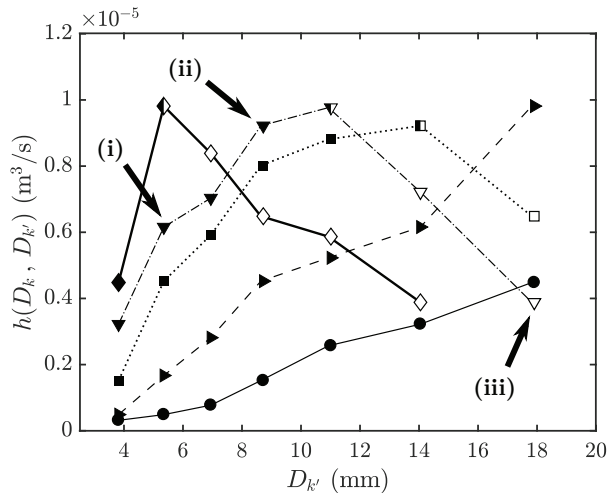


FIGURE 10. Experimental measurements of the bubble pair collision frequency, $h(D_k, D_{k'})$ obtained for the injection condition $\alpha_0 = 4.9\%$ at a stage of the evolution of the swarm where $D_{V90} = 18.25$ mm ($D_{V90}/D_0 = 4.74$). The symbols represent the different bubble classes according to Table 2. Solid symbols represent pairs of bubbles colliding in the first regime, while hollow ones denote collisions within the second regime. The series corresponding to $D_k = 6.67$ mm and $D_k = 10.90$ mm are not plotted for clarity. The points indicated by arrows correspond to the cases shown in figure 13.

analogy with the kinetic theory of gases (Vincenti & Kruger 1965). These models (see e.g. the review in Liao & Lucas 2010) generally consider h as the volume swept per unit time by the colliding bubbles. It is usually referred to as *collision kernel*, or the *coalescence kernel* if the efficiency is also included (Marchisio & Fox 2013). However, taking into account that h is symmetric, resulting in $h(D_k, D_{k'}) = h(D_{k'}, D_k)$, in the present work it will be referred to as *bubble pair collision frequency*.

The evolution of $h(D_k, D_{k'})$ is described hereafter for the experimental case corresponding to $\alpha_0 = 4.9\%$, as a representative example. Figure 10 shows the results of the bubble pair collision frequency for various bubble pairs at a stage of the evolution of the swarm where $D_{V90} = 18.25$ mm ($D_{V90}/D_0 = 4.74$). The adopted representation displays the evolution of $h(D_k, D_{k'})$ with $D_{k'}$ for the different classes of bubbles (constant values of D_k). We should remember that, according to figure 8, since the bubble size distributions evolve in a similar way for all values of α_0 , D_{V90}/D_0 can be used as a parameter to describe the coalescence cascade process. Considering the results corresponding to the smallest bubble size present in the distribution, $D_k = 3.85$ mm (●), a monotonous increment of the collision frequency is observed when the size of the other colliding bubble, $D_{k'}$, increases. This behaviour is also initially observed for larger bubbles, i.e. larger values of D_k , up to a certain value of $D_{k'}$ beyond which the frequency begins to decrease. Taking into account the interchangeability of D_k and $D_{k'}$, it can be stated that the slope of the curve $h(D_k, D_{k'}) - D_{k'}$ increases with D_k . This monotonically increasing behaviour of the bubble pair collision frequency, characterized by the fact that at least one of the bubbles involved in the collision is relatively small, will be referred to as the first regime (represented by solid symbols in figure 10). In this regime, as soon as the bubbles collide, they coalesce or (in a very few cases) bounce back, but their surfaces do not deform during a certain time until they coalesce. On the other hand, as observed for $D_k \geq 8.62$ mm (■, ▼, ◆), the evolution of the bubble pair collision frequency shows a local maximum at certain values of $D_{k'}$, which decreases as D_k increases. After this

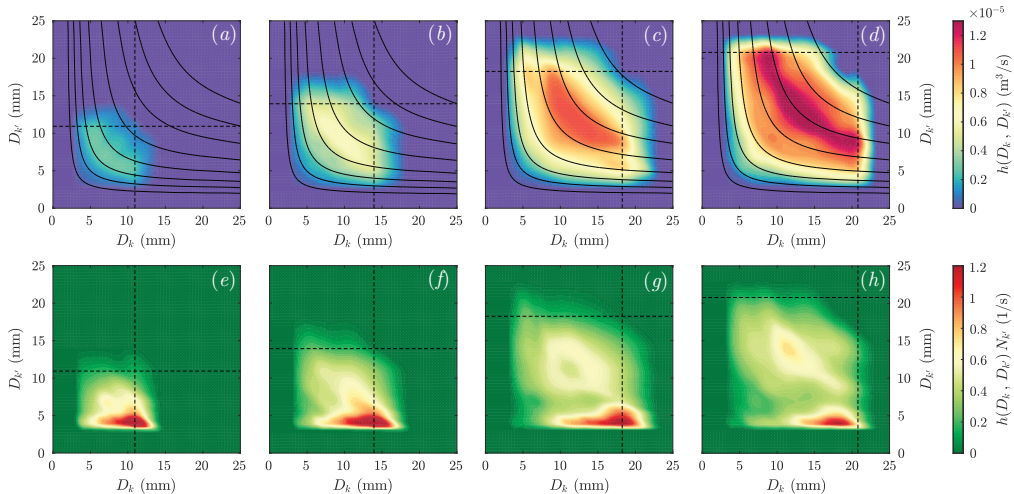


FIGURE 11. Contour plots of: (a–d) $h(D_k, D_{k'})$ and (e–h) the product $h(D_k, D_{k'}) N_{k'}$ for $\alpha_0 = 4.9\%$ at four different instants of the bubble coalescence cascade process, characterized by D_{V90} (indicated by dashed lines in each plot). (a,e) $D_{V90} = 10.93$ mm ($D_{V90}/D_0 = 2.84$); (b,f) $D_{V90} = 13.96$ mm ($D_{V90}/D_0 = 3.62$); (c,g) $D_{V90} = 18.25$ mm ($D_{V90}/D_0 = 4.74$) and (d,h) $D_{V90} = 20.79$ mm ($D_{V90}/D_0 = 5.40$). The solid black lines in (a–d) indicate constant values of the reduced diameter D_p .

552 maximum a different behaviour appears, which defines a second collision/coalescence
 553 regime (represented by hollow symbols in figure 10), where the two involved bubbles are
 554 large enough to be able to deform during the coalescence process. In this regime, once
 555 the bubbles get in touch, their interfaces deform and flatten forming a thin liquid film
 556 between the two bubbles, which mainly drains sideways (Huisman *et al.* 2012; Pavlov
 557 *et al.* 2021). The time spent on the bubbles surface deformation and on the liquid film
 558 drainage, before coalescence, increases the time during which the bubbles interact, leading
 559 to a reduction of the corresponding collision/coalescence frequency.

560 Figures 11(a–d) show the contours of $h(D_k, D_{k'})$ at four different instants of the
 561 coalescence cascade process corresponding to $\alpha_0 = 4.9\%$. In this case, bubbles of diameter
 562 $D_0 = 3.85$ mm are initially injected and, as they coalesce while they rise, a population
 563 of bubbles of increasing diameters is generated. The values of D_{V90} of the bubble size
 564 distributions corresponding to panels (a–d), indicated with horizontal and vertical dashed
 565 lines, are 10.93 mm, 13.96 mm, 18.25 mm and 20.79 mm respectively ($D_{V90}/D_0 = 2.84$;
 566 3.62; 4.74 and 5.40). The plots clearly show that $h(D_k, D_{k'})$ is a symmetric function
 567 that increases with D_{V90} . In fact, it can be observed that the coalescence frequencies
 568 between two small or two large bubbles are small compared to the collision frequency
 569 between bubbles of intermediate sizes. Note for instance that the maximum coalescence
 570 frequency in figure 11(d) falls in a fringe corresponding to the coalescence of bubbles
 571 of $D_k = 8$ mm ($D_k = 20$ mm) with bubbles of $D_{k'} = 20$ mm ($D_{k'} = 8$ mm), or to
 572 the coalescence between two bubbles of diameter $D_k = D_{k'} \approx 12$ mm. Interestingly, a
 573 close inspection of the contour plots indicates that the colour levels nearly follow lines
 574 of constant values of

$$D_p = \left[\frac{1}{2} \left(\frac{1}{D_k} + \frac{1}{D_{k'}} \right) \right]^{-1} = \frac{2D_k D_{k'}}{D_k + D_{k'}}, \quad (3.4)$$

575 drawn with solid lines in figure 11(a–d). The diameter D_p represents the diameter of a
 576 bubble whose radius of curvature is equal to the mean radius of curvature of the pair of

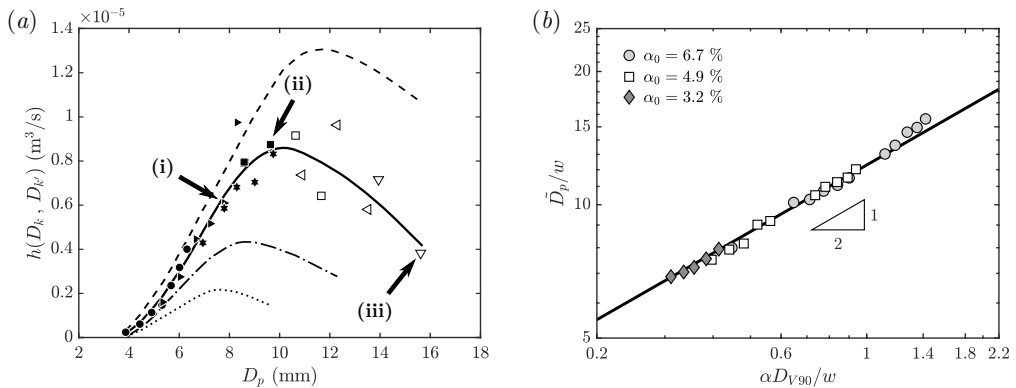


FIGURE 12. (a) Bubble pair collision frequency, $h(D_k, D_{k'})$, as a function of the reduced diameter, D_p . The symbols represent the experimental results shown in figure 10. Collisions taking place in the first regime are depicted with solid symbols, while hollow ones are used to represent collisions in the second regime. As in figure 10, the cases labeled as (i), (ii) and (iii) respectively correspond to the series (a), (b) and (c) in figure 13. Lines represent the averaged value of $h(D_k, D_{k'})$ along isolines of D_p in figure 11 for $D_{V90}/D_0 = 5.40$ (---); 4.74 (—); 3.62 (-.-) and 2.84 (⋯). (b) Dependence of \tilde{D}_p/w with $(\alpha D_{V90}/w)$ for the experimental cases tested. The solid line indicates that $\tilde{D}_p/w \propto (\alpha D_{V90}/w)^{1/2}$, according to equation (4.10). Here α is the local gas volume fraction.

577 interacting bubbles, and will be further called the reduced diameter. This diameter has
 578 been commonly used to describe the deformation of interacting bubbles and in models
 579 of drops/bubbles coalescence (Chesters & Hofman 1982; Kamp *et al.* 2001; Neitzel &
 580 Dell'Aversana 2002). In addition to $h(D_k, D_{k'})$ shown in figures 11(a–d), figures 11(e–
 581 h) display the bubble pair collision frequency weighted by the number of bubbles of
 582 size $D_{k'}$. This quantity represents the frequency of collision of a bubble of size D_k
 583 with bubbles of size $D_{k'}$ and obviously depends on the number of bubbles of size $D_{k'}$ in the
 584 distribution, $n(D_{k'})$. It represents the contribution of bubbles of class k' to the coalescence
 585 frequency of bubbles of class k , $g_c(D_k)$, as established in equation (1.7). It can be seen
 586 that $h(D_k, D_{k'}) N_{k'}$, obtained experimentally as $\Gamma_{kk'}/N_k$ is no longer symmetric and it
 587 depends on the bubbles size distribution, having the maximum values for $D_{k'} = D_0$ in
 588 our particular case, since the number of bubbles of size D_0 is larger than the number of
 589 bubbles of other sizes, as shown in figure 9.

590 A description of the bubble pair collision frequency, $h(D_k, D_{k'})$, is therefore sought after
 591 in terms of the reduced diameter, D_p . The experimental values of $h(D_k, D_{k'})$ displayed
 592 in figure 10 are represented as a function of the corresponding D_p in figure 12(a). They
 593 fall on a single curve, represented by the thick solid line, which corresponds to the
 594 averaged bubble pair collision frequency along lines of constant D_p in figure 11(c). This
 595 curve clearly indicates the existence of the two different collision regimes commented
 596 above, properly distinguished now as a function of D_p . Initially, in the first regime
 597 (solid symbols), $h(D_p)$ increases with D_p until it reaches a maximum value beyond
 598 which it begins to decrease with D_p (hollow symbols). In this figure, as in figure 10,
 599 the cases indicated by arrows correspond to the time series of experimental images
 600 shown in figure 13. Equivalent results are found for different values of D_{V90} , as shown
 601 in figure 12(a) (different lines) for the instants of the coalescence cascade presented in
 602 figure 11(a–d). This result corroborates that D_p properly captures the dependence of
 603 the collision frequency on the bubble sizes. The values of the reduced diameter at which
 604 the maximum of $h(D_p)$ occurs, i.e. the change from the first to the second collision

605 regime, denoted as \tilde{D}_p , are displayed in figure 12(b) for the different experimental cases
 606 tested. For the smallest value of the injected volume fraction, $\alpha_0 = 2.4\%$, the entire
 607 coalescence cascade took place in the first regime, without transitioning to the second
 608 one, and no data is represented in this case. It can be observed that \tilde{D}_p increases
 609 with the concentration of bubbles and with D_{V90} , following a power law given by
 610 $\tilde{D}_p/w \propto (\alpha D_{V90}/w)^{1/2}$ as it will be commented later on in §4.

611 In order to better illustrate the main characteristics of the two regimes mentioned
 612 above, different coalescence events are shown in the time series of snapshots displayed in
 613 figure 13. The time intervals between images are the same for the four series. The black
 614 dots inside the bubbles denote the instantaneous position of their centroids, while the
 615 coloured ones indicate their previous positions, describing the bubbles trajectories. The
 616 cases shown are representative of the collisions taking place during the evolution of the
 617 swarm. The first three series (figures 13a,b,c) have been selected for the same injection
 618 condition and stage of the swarm ($\alpha_0 = 4.9\%$ and $D_{V90}/D_0 = 4.74$), and correspond
 619 to the points indicated with arrows in figures 10 and 12. The processes involve pairs of
 620 bubbles where the diameter of one of them is $D_k = 13.90$ mm (\blacktriangledown), whose trajectory
 621 is represented with red dots in figure 13. The other bubbles that form the pairs have
 622 different diameters $D_{k'}$, as indicated in figure 10, and their trajectories are represented
 623 by blue dots in the corresponding panels of figure 13. On the other hand, figure 13(d)
 624 represents a coalescence event in a swarm also at $D_{V90}/D_0 \approx 4.74$, where the pair of
 625 bubbles are similar to those in figure 13(c), but at a higher void fraction, $\alpha_0 = 6.7\%$. As
 626 specifically indicated in the figure, coalescence events belonging to both regimes have been
 627 represented. The processes shown in figure 13(a,b) represent typical collisions taking place
 628 in the first regime. It can be seen that in both cases the coalescence happens as soon as the
 629 two bubbles collide, around $t = -20$ ms in both series. In these cases, the bubbles do not
 630 significantly change their shape when they interact and rapidly contact at a point before
 631 coalescing. It could be said that they *meet and kiss* each other. This type of coalescence
 632 was reported for unconfined configurations by Howarth (1964) and later on modelled as
 633 the ratio between the interfacial energy and the energy of collision (Sovova 1981; Tsouris
 634 & Tavlarides 1994). However, the collision shown in figure 13(c) is markedly different
 635 and belongs to the second regime. In this case, when the bubbles get close enough (after
 636 $t = -100$ ms) they deform and flatten, with the upper bubble surrounding the lower
 637 one. They move together for a while before being able to open a hole in the liquid film
 638 that separates them, and coalesce. During this period, the lower bubble, D_k (red dots),
 639 decelerates before contacting the upper one, $D_{k'}$ (blue dots), using its kinetic energy
 640 to deform the interface (Chesters 1991; Kamp *et al.* 2001) and to increase the pressure
 641 in the liquid film that forms between the two bubbles (Duineveld 1998). Thus, unlike in
 642 figures 13(a) and (b), the bubbles *meet and dance for a while before kissing* in figure 13(c).
 643 The dancing time increases with the size of the bubbles since large bubbles are able to
 644 deform more easily, what makes $h(D_k, D_{k'})$ decrease in the second regime. It is worth
 645 noting that in the earlier stages of the cascade process, i.e. for low values of D_{V90} , the
 646 swarm is formed by relatively small bubbles which collide exclusively in the first regime.
 647 The time the bubbles take to deform and adapt their shapes before coalescing not only
 648 depends on their sizes but also on the liquid velocity fluctuations, induced by the motion
 649 of the bubbles in the swarm. Larger velocity fluctuations favour the destabilization of the
 650 liquid film separating the contacting bubbles and thus, their coalescence. To illustrate this
 651 effect, figure 13(d) shows a pair of bubbles similar to those in figure 13(c) in a bubble
 652 swarm also characterized by $D_{V90} \approx 18.25$ mm ($D_{V90}/D_0 \approx 4.74$), but with higher
 653 concentration of bubbles, $\alpha_0 = 6.7\%$. In this case, although the interacting bubbles are

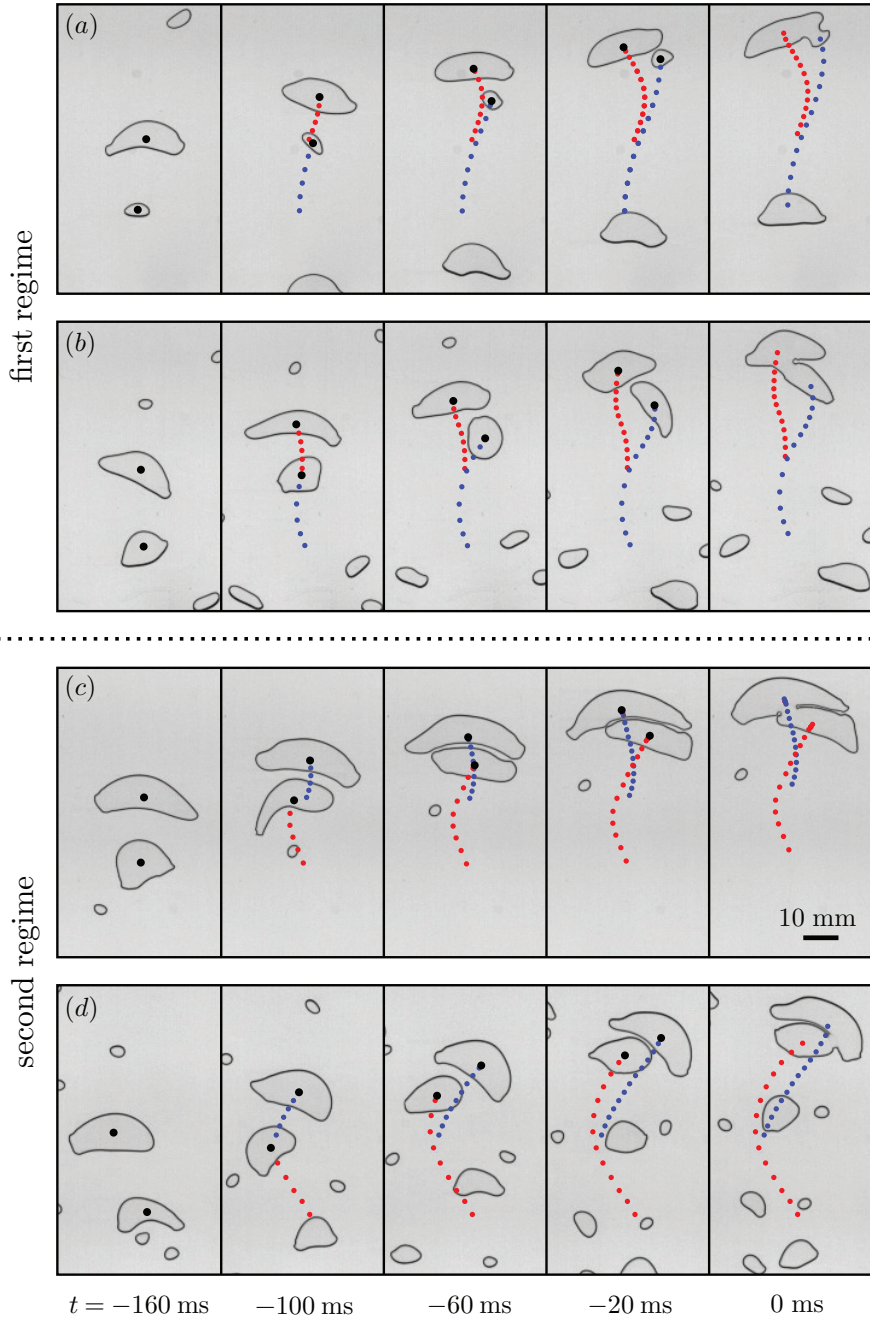


FIGURE 13. Images showing the time evolution of representative cases of the collision process at a stage of the evolution of the swarm where $D_{V90} = 18.25$ mm ($D_{V90}/D_0 = 4.74$) for $\alpha_0 = 4.9\%$. They correspond to the cases denoted by (i), (ii) and (iii) in figures 10 and 12a, with (a) $D_p = 7.86$ mm, (b) $D_p = 9.64$ mm, (c) $D_p = 15.55$ mm. In (d), the bubbles belong to classes $k = 5$ and $k' = 6$ (Table 2) with $D_p = 15.87$ mm and for $\alpha_0 = 6.7\%$. The instantaneous location of the centroids of the bubbles are indicated with black dots. The position of the centroids in previous frames describing the trajectories of the bubbles are represented by sequences of coloured dots (only one out of three instants are plotted for clarity). The time to coalescence in each snapshot is indicated at the bottom of the figure.

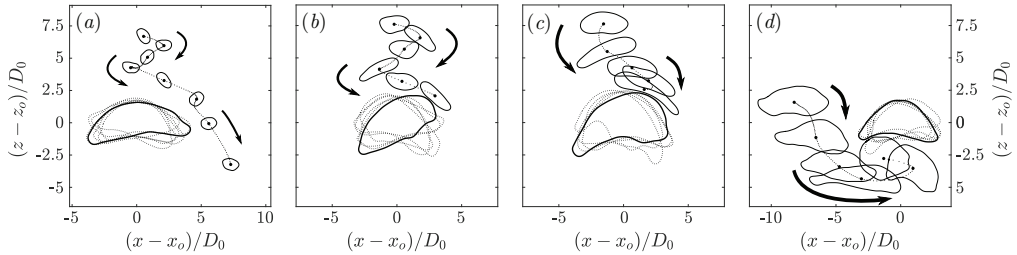


FIGURE 14. Effect of bubble deformation in the first collision regime, illustrated by different characteristic interaction events of a small bubble of size $D_{k'}$ with a larger one of size D_k , placed at the origin of coordinates, for (a) $D_p = 8.33$ mm, (b) $D_p = 9.68$ mm, (c) $D_p = 11.59$ mm and (d) $D_p = 12.11$ mm. The bubble swarm corresponds to $D_{V90} = 23.17$ mm ($D_{V90}/D_0 = 6.02$) and $\alpha_0 = 4.9$ %. Both coordinates have been normalized by the corresponding bubble injection diameter D_0 . The arrows indicate the direction of the relative motion of $D_{k'}$.

654 similar to those displayed in panel (c), the coalescing time is shorter because the liquid
 655 fluctuation velocities are larger for $\alpha_0 = 6.7$ % than for $\alpha_0 = 4.9$ %. In fact, it can be
 656 observed in figure 13 that at $t = -160$ ms the distance between the centroids of the
 657 two bubbles is larger in (d) than in (c). Therefore, it can be asserted that the global
 658 motion of the swarm is driven by buoyancy and, thus, governed mainly by the evolving
 659 bubble size distribution, characterized by D_{V90} , and the concentration of bubbles, α_0
 660 (see discussion of figure 6b in §3.1). Furthermore, the bubble collision rate increases with
 661 the liquid perturbation velocity which increases as the bubbles coalesce and get larger,
 662 i.e. as D_{V90} increases.

663 The role played by hydrodynamic interactions on the coalescence process is also
 664 illustrated in figure 14, now considering different events where the smallest bubble is
 665 above the largest one. In the figure, typical situations of bubbles interacting in the first
 666 regime are presented for different values of D_p , in a bubble swarm corresponding to
 667 $\alpha_0 = 4.9$ % and $D_{V90} = 23.17$ mm ($D_{V90}/D_0 = 6.02$). The relative location of the
 668 smallest bubble of the pair, $D_{k'}$, is plotted as it interacts with a larger bubble, D_k . The
 669 origin of coordinates (x_o, z_o) corresponds to the centroid of bubble D_k at
 670 each instant. The temporal evolution of the relative position of the centroid of bubble
 671 $D_{k'}$, between the represented stages, is indicated by dots. Bubble pairs for increasing
 672 values of D_p (and of $h(D_k, D_{k'})$) are presented in figures 14(a-c). For a nearly constant
 673 value of D_k (largest bubble), the size $D_{k'}$ (smallest bubble) is progressively increased
 674 from left to right. In figure 14(a), illustrating the interaction of a small bubble with a
 675 big one, the small bubble barely deforms, and is ejected away from the larger one due
 676 to the overpressure established around its stagnation point. Consequently, this case is
 677 not considered as a collision in our analysis (see §A.1) and the collision frequency of
 678 this type of bubbles is low. As $D_{k'}$ increases (figure 14b,c), in addition to increasing
 679 the possible length of interaction with bubble D_k , the capability of $D_{k'}$ to be deformed
 680 also increases, favouring the collision between both bubbles. Besides the hydrodynamic
 681 mechanisms governing the response of bubble $D_{k'}$ to the flow around the top of bubble
 682 D_k , additional bubble deformation effects have been also observed when the two bubbles
 683 are sufficiently large (figure 14d). In this kind of collisions, the liquid velocity field brings
 684 the bubbles sufficiently close so that bubble $D_{k'}$ deforms towards the low pressure area
 685 of the wake of bubble D_k . Indeed, these final instants of the interaction process, based on
 686 the wake entrainment mechanism, lead to bubble collision when the interacting bubbles
 687 are large enough to deform (Miyahara *et al.* 1991). In contrast, smaller bubbles that

688 barely deform and respond faster to the liquid velocity fluctuations can eventually avoid
689 the collision (Filella *et al.* 2020).

690 In figures 13(*a,b*), the discussion was focused primarily on the short time interaction,
691 as well as on the wake effects of the bubbles once they were carried out close enough by
692 the liquid motion. In contrast, the configurations shown in figures 14(*a-d*) focus on the
693 response of $D_{k'}$ to the hydrodynamic effects caused by its interaction with bubble D_k .
694 They illustrate the influence of the bubble sizes, and of their capability to be deformed,
695 on the increase of h with D_p in the first regime. The cases shown in figures 13 and 14
696 are representative of the collision phenomenology observed in the coalescence cascade
697 process and contribute equally to the bubble pair collision frequency obtained from the
698 experiments.

699 4. Formulation of the coalescence model

700 To model the rate of change of the population of bubbles due to coalescence, \dot{Q}_c , in
701 equation (1.2), it is necessary to implement models for the integral kernels involved in
702 the coalescence rate in equation (1.5), which consider the interaction between bubbles
703 of different sizes, namely D_k and $D_{k'}$, respectively. In this sense, it has to be taken into
704 account that bubble coalescence includes a first approaching step, starting at distances
705 typically larger than the bubble sizes, driven by the local transport mechanisms. Sub-
706 sequently, a second step, characterized by the short-distance bubble-bubble interaction,
707 takes place (Marchisio & Fox 2013). The whole process is commonly modelled considering
708 both stages separately, the first accounting for the bubble collision frequency $h(D_k, D_{k'})$
709 and the second for the coalescence efficiency term $\lambda(D_k, D_{k'})$. The efficiency is usually
710 expressed comparing the time required to drain and disrupt the liquid film formed
711 between the two bubbles when they collide, t_d , with the time the bubbles remain in
712 contact under the influence of the external flow, i.e. the residence time \bar{t}_c .

713 As mentioned above, in the two-dimensional confined configuration of interest here,
714 the coalescence efficiency λ , has been defined as the fraction of pairs of colliding bubbles
715 which end up coalescing. In this case, once the bubbles collide, they cannot move away
716 in the direction perpendicular to the walls and, in most of the cases, eventually coalesce.
717 Thus, the coalescence efficiency is high and nearly constant, being thus independent of
718 the size of the colliding bubbles and of the external flow conditions, such as D_{V90} or α_0
719 (figure 4). Consequently, the bubble collision frequency $h(D_k, D_{k'})$ will be considered as
720 the bubble coalescence frequency since both functions behave in the same way and, in the
721 following, we will focus on developing a model for $h(D_k, D_{k'})$, which jointly accounts for
722 the local transport phenomena and for the effects derived from the bubbles deformations
723 and their hydrodynamics interaction when they approach.

724 In general, $h(D_k, D_{k'})$ has been modelled as a characteristic relative velocity between
725 the two colliding bubbles, $\bar{u}_r(D_k, D_{k'})$, multiplied by a characteristic cross-sectional
726 collision area $S_c(D_k, D_{k'})$, which usually depends on the size of the colliding bubbles,

$$h(D_k, D_{k'}) \sim S_c \bar{u}_r. \quad (4.1)$$

727 In particular, Coualoglou & Tavlarides (1977) proposed an expression for $h(D_k, D_{k'})$
728 based on the collision of molecules in kinetic theory of gases, given by

$$h(D_k, D_{k'}) \sim \frac{\pi}{4} (D_k + D_{k'})^2 [u^2(D_k) + u^2(D_{k'})]^{1/2}, \quad (4.2)$$

729 where $u(D_k)$ and $u(D_{k'})$ are the root-mean-square of the velocity fluctuations of bubbles
730 of sizes D_k and $D_{k'}$, respectively. The relative velocity between the two bubbles can be

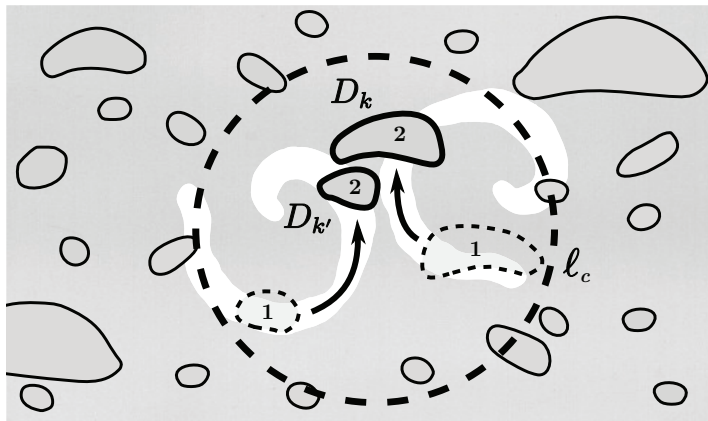


FIGURE 15. Sketch illustrating a typical collision event between two bubbles of sizes D_k and $D_{k'}$, corresponding to a reduced diameter falling within the first regime. The initial positions of both bubbles of the pair are represented with dashed lines and labeled with number 1. The actual positions of the swarm is depicted with solid lines, being the colliding bubbles labeled with number 2. The white flow structures represent the swarm-induced agitation in the liquid. The dashed circle indicates the effective interaction length between the two bubbles, $\ell_c \sim D_{V90}/\alpha$.

731 established by different mechanisms, depending on the liquid field where the bubbles are
 732 immersed, i.e. turbulent fluctuations of the carrier fluid, size-dependent differences in
 733 the bubble rising velocities, wake entrainment or shear-layer induced velocity differences,
 734 among others. However, in the present flow where the liquid velocity is not externally
 735 imposed, the mean motion of the swarm and its agitation are driven by gravity effect
 736 and, thus, the mechanisms controlling the relative approaching velocity must be related
 737 to the distribution of sizes in the population of bubbles. Under the present conditions,
 738 the liquid fluctuating velocities are generated by the interaction of all the bubbles, whose
 739 sizes range from D_0 to the largest ones, represented by the characteristic diameter D_{V90} .
 740 Experimental observations suggest that the swarm-induced agitation (represented by the
 741 *white eddies* in the sketch shown in figure 15) is the mechanism that controls the approach
 742 of a pair of bubbles. This mechanism is dominant compared to any other mechanism,
 743 such as wake entrainment or buoyancy-induced velocity difference between bubbles of
 744 different sizes. The relative bubble approaching velocity, \bar{u}_r , will be thus assumed to be
 745 the standard deviation of the bubbles velocities, which in the present case is proportional
 746 to the liquid velocity fluctuations induced by the largest bubbles in the swarm,

$$\bar{u}_r(D_k, D_{k'}) \sim \alpha^{0.46} \sqrt{gD_{V90}}. \quad (4.3)$$

747 The effect of the concentration of bubbles, α , has been included in equation (4.3),
 748 according to Bouche *et al.* (2012) for a monodispersed confined swarm of bubbles. Such
 749 relative velocity can be understood as the fluctuating velocity associated with the *integral*
 750 *scale* of the self-induced agitation, as it is produced by the largest and more intense
 751 bubbles.

752 Concerning the cross-sectional collision area, experimental observations of the collision
 753 phenomena indicate that, for a couple of bubbles to collide, they must be within a certain
 754 maximum distance. This characteristic length, ℓ_c , defines a region of the cell plane where
 755 the liquid velocity fluctuations generated by the bubble swarm are correlated and are able
 756 to bring the bubbles together (represented by a dashed circle in the sketch of figure 15).

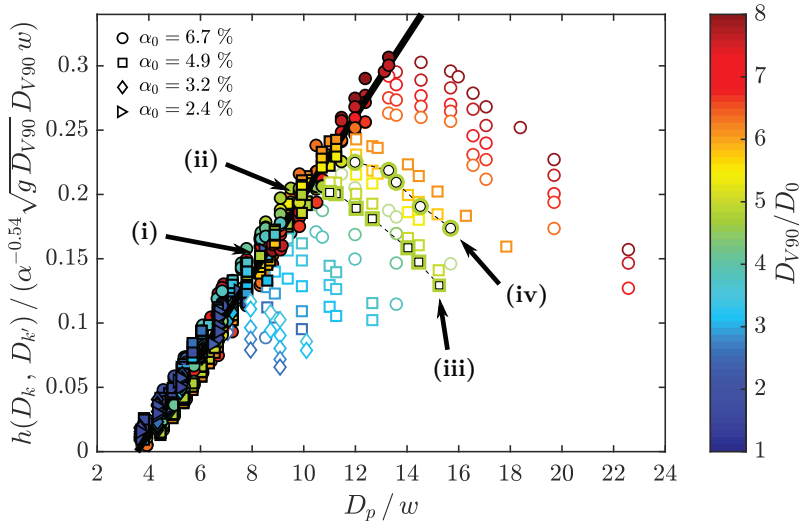


FIGURE 16. Dimensionless bubble pair coalescence frequency versus D_p/w , according to equation (4.7). Colored symbols represent the different stages of the coalescence cascade process, i.e. different values of D_{V90}/D_0 . The coalescence events falling within the second regime have been represented with hollow symbols. The series of points highlighted with dashed lines indicate stages of the size distribution with similar values of D_{V90}/D_0 but for two different values of α_0 . The cases denoted by (i), (ii), (iii) and (iv) corresponds to the respective panels (a), (b), (c) and (d) of figure 13. The solid line indicates a linear fit of the data within the first regime, given by $0.031D_p/w - 0.109$.

757 Under these considerations, $S_c(D_k, D_{k'}, \ell_c)$ can be expressed as

$$S_c(D_k, D_{k'}, \ell_c) \sim \ell_c w \hat{F}\left(\frac{D_p}{w}\right), \quad (4.4)$$

758 where w is included for dimensional consistency. Here, \hat{F} is a dimensionless function that
 759 depends on the reduced diameter of the pair of bubbles, and accounts for the capability
 760 of the bubbles to be deformed. In equation (4.4), the characteristic length of influence
 761 of the external mechanisms transporting the bubbles, ℓ_c , is proportional to the *integral*
 762 *scale* of the liquid flow, D_{V90} . Therefore, this influence length varies as the distribution
 763 of sizes evolves with the vertical position. The local concentration of bubbles, however,
 764 is expected to affect this correlation length, for instance by inducing a screening effect
 765 due to successive passages of bubbles. In fact, Alm eras *et al.* (2018) reported that for
 766 void fractions $\alpha \geq 5\text{--}6\%$ within monodispersed swarms of bubbles of size $d \sim D_0$, the
 767 correlation length for dye transport scaled with the mean distance between two bubbles
 768 which is given by d/α . It can therefore be presumed that for polydispersed swarms, the
 769 wide distribution of sizes may, in fact, decrease the values of the gas volume fraction
 770 from which the correlation length shortening occurs. Therefore, it can be considered that
 771 a pair of bubbles can be transported close to each other if they are initially separated by
 772 a distance shorter than

$$\ell_c(z) \sim \frac{D_{V90}(z)}{\alpha(z)}, \quad (4.5)$$

773 being its variation with the position determined in turn by the changes of the population
 774 of bubbles. Substituting (4.5) into (4.4), one gets

$$S_c(D_k, D_{k'}) \sim \frac{D_{V90}}{\alpha} w \hat{F}\left(\frac{D_p}{w}\right). \quad (4.6)$$

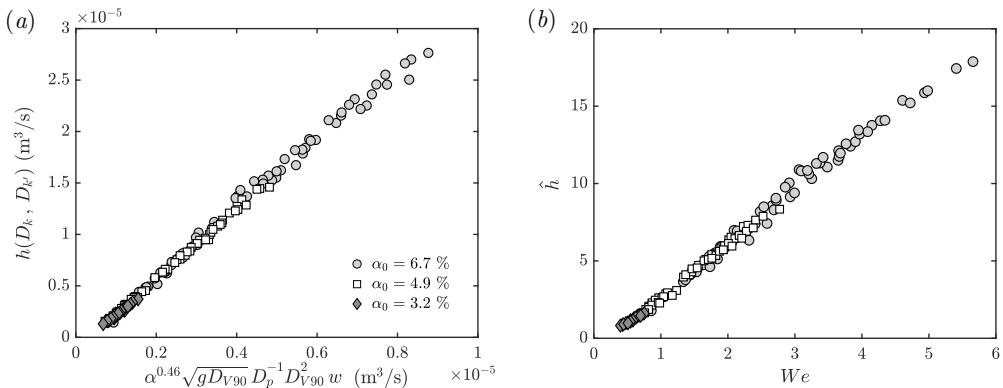


FIGURE 17. (a) Experimental values of $h(D_k, D_{k'})$ in the second regime for $\alpha_0 = 3.2\%$, 4.9% and 6.7% respectively, versus the model given by expression (4.9). Here $h(D_k, D_{k'}) = 3.41 (\alpha^{0.46} \sqrt{g D_{V90}} D_{V90} w D_{V90} / D_p - 3.2 \times 10^{-7})$. (b) Dimensionless bubble pair coalescence frequency in the second regime versus the Weber number, $We = \rho \alpha^{0.92} (g D_{V90}) D_p / \sigma$.

775 In order to determine \hat{F} , the values of $h(D_k, D_{k'})$ divided by $\alpha^{-0.54} \sqrt{g D_{V90}} D_{V90} w$
 776 have been represented in figure 16 as a function of the normalized reduced diameter,
 777 D_p/w . It is shown that, for the collision events falling in the first regime (solid symbols),
 778 the values of the normalized frequency collapse on a single curve, following a linear
 779 dependence with D_p/w . Therefore, it can be concluded that \hat{F} is a linear function of
 780 D_p/w for the pairs of bubbles colliding in the first regime, leading to the following
 781 scaling law for the collision frequency

$$h \sim \alpha^{-0.54} \sqrt{g D_{V90}} D_{V90} w \frac{D_p}{w}. \quad (4.7)$$

782 Only some moderate data scattering can be noticed for the first regime around this linear
 783 curve (solid line in figure 16), revealing that the main physics controlling the process is
 784 captured by equation (4.7). In this sense, (4.3) and (4.5) properly scale the magnitude
 785 of the self-induced liquid velocity fluctuations and the interaction region for a pair of
 786 bubbles, driving the transport of the bubbles during their approach. In addition, the
 787 function $\hat{F} \propto D_p/w$ includes the bubble size dependence and accounts for the bubbles
 788 deformation process as they interact (see figures 13 and 14).

789 On the other hand, as expected from the experimental results described in §3.2, a
 790 clear deviation is observed for the collision events taking place in the second regime
 791 (hollow symbols in figure 16). These events happen for values of D_p/w larger than the
 792 corresponding \tilde{D}_p/w , established at each stage of the evolution of the swarm for the
 793 different α_0 (figure 12b) and, thus when both bubbles are relatively large, i.e. close
 794 to D_{V90} . In this second regime, most of the coalescence time is spent on the bubbles
 795 deformation process, being the approaching time of the bubbles a small fraction of the
 796 total time. We further assume that the bubbles deform and adapt their shapes due to
 797 the mean local strain (see figure 13c)

$$s \sim \frac{\bar{u}_r}{2} \left(\frac{1}{D_k} + \frac{1}{D_{k'}} \right) = \frac{\alpha^{0.46} \sqrt{g D_{V90}}}{D_p}, \quad (4.8)$$

798 acting in a volume enclosing the pair of bubbles $V_c \sim D_{V90}^2 w$. Thus, the bubble pair

799 collision frequency can be estimated by $h(D_k, D_{k'}) \sim s \times V_c$, providing

$$h(D_k, D_{k'}) \sim \alpha^{0.46} \sqrt{gD_{V90}} D_{V90} w \frac{D_{V90}}{D_p}. \quad (4.9)$$

800 Equation (4.9) indicates that, in the second regime, $h(D_k, D_{k'})$ decreases as D_p/w
 801 increases as shown in figure 16. Figure 17(a) shows the experimental values of the bubble
 802 pair coalescence frequency that fall in the second regime versus the model given by
 803 equation (4.9), exhibiting an excellent agreement. In fact, matching equations (4.7) and
 804 (4.9), it can be inferred that

$$\frac{\tilde{D}_p}{w} \propto \left(\frac{\alpha D_{V90}}{w} \right)^{1/2}, \quad (4.10)$$

805 as shown in figure 12(b). Furthermore, since the bubble pair Weber number,
 806 $We = \rho \tilde{u}_\tau^2 D_p / \sigma$, has been typically used to describe the drainage and rupture of
 807 the liquid film in drops/bubbles coalescence models (Chesters & Hofman 1982),
 808 equation (4.9) can also be expressed in dimensionless form in terms of the Weber
 809 number as

$$\hat{h} = h(D_k, D_{k'}) \frac{\rho \alpha^{0.46} \sqrt{gD_{V90}}}{w\sigma} \frac{D_p^2}{D_{V90}^2} \sim We, \quad (4.11)$$

810 where $We = \rho \alpha^{0.92} (gD_{V90}) D_p / \sigma$. The experimental values of $\hat{h}(We)$ are shown in
 811 figure 17(b) versus the Weber number for $\alpha_0 = 3.2\%$, 4.9% and 6.7% , respectively.
 812 Again, the agreement between the experimental measurements and the model propose
 813 by equation (4.11) is excellent, following a linear dependence of \hat{h} with We . In addition
 814 to the different mechanisms driving the coalescence of bubbles in both regimes, resulting
 815 in the models proposed in (4.7) and (4.9), it is worth noting that the contribution of both
 816 types of collisions to the global evolution of the swarm is also quite different. In fact,
 817 given that the number of large bubbles in the swarm is considerably low, the contribution
 818 to bubble coalescence within the second regime is less significant than that in the first one
 819 (figures 11e–h). However, the coalescence events in the second regime lead the evolution
 820 of the tails of the distribution of sizes. This type of coalescence generates even larger
 821 bubbles, which in turn eventually establish the velocity and length scales governing the
 822 coalescence cascade process.

823 Finally, the effect of the bubble pair collision frequency on the evolution of the
 824 coalescence cascade process can be generally assessed examining the results of the global
 825 evolution of the swarm displayed in figure 5. Indeed, the mean collision frequency $\langle h \rangle_\infty$
 826 in the swarm can be obtained considering the mean coalescence frequency $\langle g_c \rangle_\infty$ and the
 827 total number of bubbles in the population N_∞ , which assuming a constant efficiency λ_∞ ,
 828 reduces to $\langle h \rangle_\infty = \langle g_c \rangle_\infty / (N_\infty \lambda_\infty)$. This mean bubble pair collision frequency represents
 829 the averaged frequency at which a bubble collides with other bubble of any size, that
 830 according to the PBE can be determined as

$$\langle h \rangle_\infty = \frac{1}{N_\infty^2 \lambda_\infty} \int_0^\infty \left[\int_0^\infty \lambda(D, D') h(D, D') n(D') dD' \right] n(D) dD, \quad (4.12)$$

831 where D and D' represent the diameters of bubbles whose corresponding volumes are v
 832 and v' respectively. Figure 18 shows that $\langle h \rangle_\infty$ follows a $3/2$ power law with D_{V90} , as
 833 inferred from equation (4.7), for the collisions of bubbles in the first regime. This result
 834 suggests that most of the collisions controlling the evolution of the number of bubbles in
 835 the swarm take place in the first regime, according to the large amount of small bubbles
 836 in the distribution (figure 9). However, it has been observed that $\langle h \rangle_\infty$ slightly increases

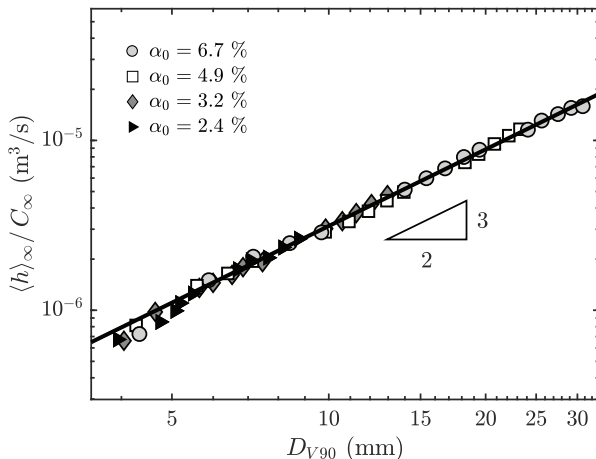


FIGURE 18. Mean collision frequency $\langle h \rangle_\infty$, averaged over all the bubble sizes present in the swarm at each stage of its evolution, as a function of the corresponding D_{V90} . The values of $\langle h \rangle_\infty$ are divided by a constant $C_\infty(\alpha_0)$ where $C_\infty = 0.163$; 0.225; 0.362 and 0.381 for $\alpha_0 = 2.4\%$; 3.2%; 4.9% and 6.7%, respectively. The thick solid line represents the expression $\sqrt{gD_{V90}D_{V90}w}$, showing the slope 3/2 as a function of D_{V90} , characteristic of the collisions taking place in the first regime.

837 with α_0 , most likely due to a combined, integral effect of the volume fraction of bubbles
 838 on the bubble size distribution in equation (4.12), $n(D)$, and of the increased relevance of
 839 the coalescence events occurring in the second regime with α_0 . Thus, in figure 18, $\langle h \rangle_\infty$
 840 has been divided by a constant, $C_\infty(\alpha_0)$, that slightly increases with α_0 .

841 5. Conclusion

842 The bubble coalescence cascade has been analyzed for a high-Reynolds number confined
 843 swarm. Bubble-induced agitation is the main mechanism driving the process, which
 844 in turn is highly dependent on the bubble size distribution. In this configuration, a
 845 significant evolution of the bubble population is observed, with sizes that grow from the
 846 injected bubble size up to 10 times larger, even for the moderate gas volume fractions
 847 tested (up to 6.7 %).

848 A detailed characterization of the coalescence process has been performed by direct
 849 observation of the coalescence events taking place in the swarm. In particular, the bubble
 850 pair collision frequency and the coalescence efficiency have been measured. Due to the
 851 confinement, the coalescence efficiency is considerably high and nearly constant in the
 852 present configuration. Thus, the bubble pair coalescence frequency is proportional to the
 853 collision frequency and we can talk indistinctly of any of them. This result motivated
 854 us to focus our attention on the collision frequency in order to elucidate the underlying
 855 physics of coalescence as a global process. Such process includes a first agitation-driven
 856 approach of a pair of bubbles and a subsequent drainage and rupture of the liquid film
 857 separating the two bubbles before they coalesce.

858 Comparing the downstream evolution of initially monodispersed bubble populations,
 859 obtained for various injected gas volume fractions, it has been shown that the dis-
 860 tributions of sizes evolve following a similar cascade of coalesce events which can be
 861 characterized, independently of the concentration of bubbles, by D_{V90} representing a

862 typical size of the largest bubbles in the distribution. However, the rate of change of the
863 size distribution depends on the bubble concentration.

864 We provide experimental evidence that three parameters control the bubble pair
865 collision/coalescence frequency, $h(D_k, D_{k'})$. These are the bubble pair reduced diameter,
866 D_p , which accounts for the bubble-pair deformation, the diameter D_{V90} and the local
867 gas volume fraction α , both characterizing the population of bubbles and the resulting
868 agitation. The interplay of these parameters is however complex and two different regimes
869 of coalescence have been identified. For low values of D_p , the bubbles are first transported
870 close to each other by the agitation induced in the swarm and as soon as they get close,
871 they collide and eventually coalesce. In this first regime, $h(D_k, D_{k'})$ increases linearly
872 with D_p . In contrast, for larger values of D_p , pairs of relatively large bubbles interact in
873 a regime mainly controlled by the bubble deformation dynamics. In this case, once the
874 bubbles are close, they elongate and deform adapting their shape as they move together
875 before being able to break the liquid film that separates them, and coalesce. In this
876 second regime, $h(D_k, D_{k'})$ decreases with D_p . The characteristic velocity governing the
877 coalescence process is considered to be associated with the *integral scale* of the liquid
878 motion induced by the largest bubbles in the swarm. This velocity has been estimated as
879 $\alpha^{0.46} \sqrt{gD_{V90}}$, which includes the effect of the local concentration of bubbles according to
880 Bouche *et al.* (2012). We conjectured that the coalescence interaction surface is associated
881 with a correlation length of the swarm-induced agitation defined by the successive pas-
882 sages of bubbles across otherwise correlated motions as $\ell_c \sim D_{V90}/\alpha$. Thus, the bubble
883 pair collision frequency in the first regime scales as $h(D_k, D_{k'}) \sim \alpha^{-0.54} \sqrt{gD_{V90}} D_{V90} D_p$
884 for $D_p/w \geq 3.52 \approx D_0/w$. However, in the second regime, observed for bubble pairs of
885 reduced diameter greater than \tilde{D}_p provided in relation (4.10), most of the coalescence
886 time is dedicated to deform the bubbles and adapt their surface to each other due to
887 the strain induced by the liquid field, given by $\alpha^{0.46} \sqrt{gD_{V90}}/D_p$. Consequently, in the
888 second regime, $h(D_k, D_{k'}) \sim \alpha^{0.46} \sqrt{gD_{V90}} D_{V90}^2 w/D_p$, characterized by the product of
889 the strain rate and the characteristic interaction volume, $V_c \sim D_{V90}^2 w$. The dependence
890 of the collision frequency in both regimes on the diameter of the largest bubbles, D_{V90} ,
891 and on the gas volume fraction, α , strongly supports the idea that the overall excitation
892 of collisions is a consequence of swarm-induced agitation and not of the relative terminal
893 velocities of the bubbles. The velocity fluctuations of the liquid agitate the bubbles, and
894 depending on their respective sizes, and consequently on D_p , they collide in one or the
895 other regime.

896 Our results indicate that D_{V90} is essential to understand the bubble cascade process
897 in the present study. In fact, it characterizes the evolution of the population of sizes, but
898 it also mainly drives the self-induced agitation in the swarm that controls the evolution
899 of the bubble population. Regardless, as these confined flows are characterized by lightly
900 interacting wakes of bubbles, it would be interesting to explore if D_{V90} also plays such
901 a relevant role in a swarm of bubbles free to move in an unconfined volume of liquid
902 when the Reynolds number of their relative motion is moderate. In that sense, it is
903 expected that the behaviour of confined swarms differ from that of unconfined ones, not
904 only because of the reduced mobility of the bubbles one around the other in a pair,
905 but also because their hydrodynamics are quite different. However, considering that the
906 characteristic fluctuating velocity is that induced by the largest bubbles in the swarm, as
907 proposed in expression (4.3), we believe that the proposed models may remain partially
908 valid for 3D inertial swarms of bubbles. Also the role played by D_p will be relevant
909 in 3D flows, although the dependency may be different due to the additional degree of
910 freedom of the bubble motion. In this regard, the cross-sectional collision area given in

(4.6) or the enclosing volume defined for the collisions in the second regime, included in (4.9), should be redefined in the three-dimensional configuration. Nonetheless, the two-dimensional configuration analyzed here has very promising applications, such those concerning light-activated reactions or cultivation of micro-algae, among others. In a future work, we plan to investigate the agitation in the swarm, which plays a crucial role in the coalescence cascade. We also plan to apply the models developed here to describe the evolution of the bubble size distribution in confined swarms with different distributions of sizes at the injection point.

Funding

This work has been partially supported by the Spanish MINECO and European Funds under projects DPI2017-88201-C3-2-R and by the Programa Operativo FEDER Andalucía 2014-2020 and Consejería de Economía y Conocimiento de la Junta de Andalucía under project 1263528. This work has also been financially supported by the French Agence Nationale de la Recherche (ANR) under reference ANR-19-CE43-0002-02 (ALLIGATOR project). JRR wants to acknowledge the Spanish MINECO for the financial support provided by the Fellowship BES-2015-071329. Support from the Red Nacional para el Desarrollo de la Microfluídica, RED2018-102829-T, is also acknowledged.

Declaration of Interests

The authors report no conflict of interest.

Appendix A

A.1. Image processing methods for bubble detection and classification

Since, even the smallest bubbles in the swarm are already larger than the thickness of the cell, the surface of each bubble is mainly perpendicular to the direction of the light, showing up in the images as a region of connected pixels with a gray level similar to that of the liquid background, enclosed by a thin dark stripe representing the air-water interface not aligned with the cell plane (figure 19a). The thickness of the dark line that delimits the perimeter of the bubble is almost constant, regardless of its size, because the curvature of the bubble in a plane perpendicular to the field of view is constant. (Bongiovanni *et al.* 2000). Detailed images of isolated bubbles within the same experimental facility and for the same range of sizes reached in this work can be found in Roig *et al.* (2012). Using this property, each image is analyzed making use of a specifically developed image processing algorithm, followed by a bubble detection and classification method. The processing algorithm involves a first pre-processing step, followed by a second one where the image is binarized. Once the bubbles present in each image are detected, their centroid positions as well as their projected areas are measured. Figure 19 shows an example of the processing steps in one of the measuring windows.

The first step of the process implies the improvement of the contrast of the original grayscale image (figure 19a). It involves the subtraction of a background reference image without bubbles and the normalization of the image brightness by correcting each value of the pixel intensity matrix. More detailed information regarding the brightness correction method can be found in Fu & Liu (2016). This brightness normalization reduces the uncertainties due to the variation of the illumination conditions and facilitates the next binarization step. Figure 19(b) shows an inversion of the resulting corrected image, where

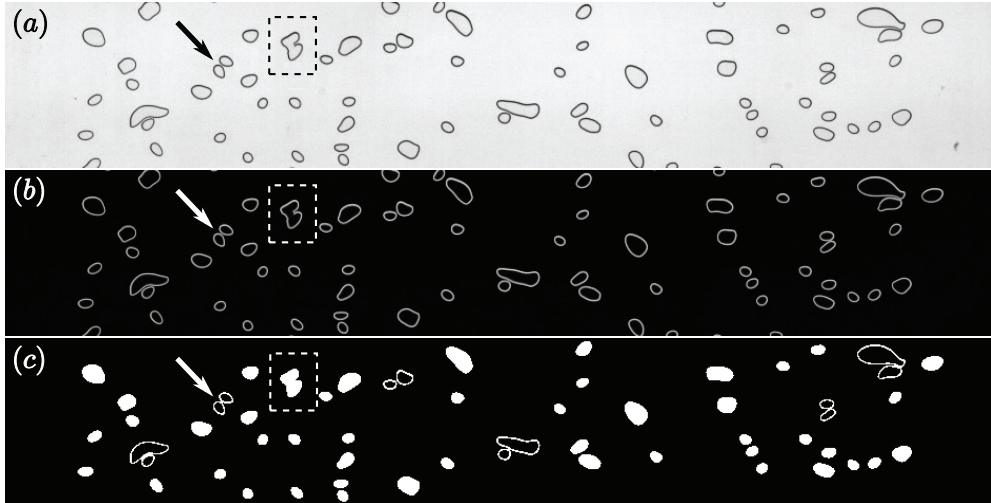


FIGURE 19. Example of the image analysis algorithm showing the two-step binarization process. (a) Original grayscale image. (b) Inversion of the pre-processed image showing the brightness normalization and the improved gray-level gradient between the bubbles edges and the background. (c) Binarized image where the bubbles have been classified as *single* bubbles (filled objects) or as *in-collision* bubbles (hollow objects). A typical bubble collision is pointed by an arrow and a recently coalesced bubble is highlighted by the box with dashed frame.

954 any physical noise (e.g. glass wall scratches and background noise) has been removed
 955 while the gray-level gradient between the bubbles edges and the background has been
 956 enhanced. Afterwards, the well-known Otsu's method (Otsu 1979) is used in the second
 957 step as an automatic, robust, global binarization-threshold selection technique.

958 After binarization, single bubbles can be detected as blobs of connected low-level pixels
 959 enclosed by unique edges of high-level pixels which are totally surrounded by background.
 960 Bubbles involved in a collision share the same edge of connected high-level pixels, however
 961 there exists an independent blob of low-level pixels for each bubble. Unlike in other works
 962 which deal with bubble collisions or formation of clusters through a separation distance
 963 criteria (see Figueroa-Espinoza & Zenit 2005; Figueroa-Espinoza *et al.* 2018, for example),
 964 the contact of at least one edge pixel of each bubble is required in the present work to
 965 define a collision. This definition is crucial, since it determines the measurement of the
 966 collision rate and the efficiency of coalescence. Figure 19(c) shows detected single bubbles
 967 as filled objects and colliding bubbles as hollow ones. This procedure to detect the bubble
 968 collisions allows us to clearly distinguish between two independent bubbles involved in a
 969 collision (see the example highlighted by an arrow in figure 19) and the newborn ones,
 970 just formed due to the coalescence of two colliding bubbles (boxed by dashed lines in
 971 figure 19).

972 Once the bubbles have been detected and classified as *single* or *in-collision* bubbles,
 973 their instantaneous characteristics are determined. The bubble position is obtained as
 974 the centroid position of the in-side blob of low-level pixels. The projected area is defined
 975 as the area occupied by the pixels belonging to the in-side blob plus those belonging to
 976 the edge. A difficulty arises obtaining the area of the bubbles involved in collisions, since
 977 the pixels composing the edge of the agglomerate are shared among the colliding bubbles.
 978 To deal with this issue, the total area of the agglomerate edge is distributed among the
 979 bubbles according to the ratio between the number of pixels enclosing the inner perimeter
 980 of each bubble and those composing the outer perimeter of the agglomerate. Since the

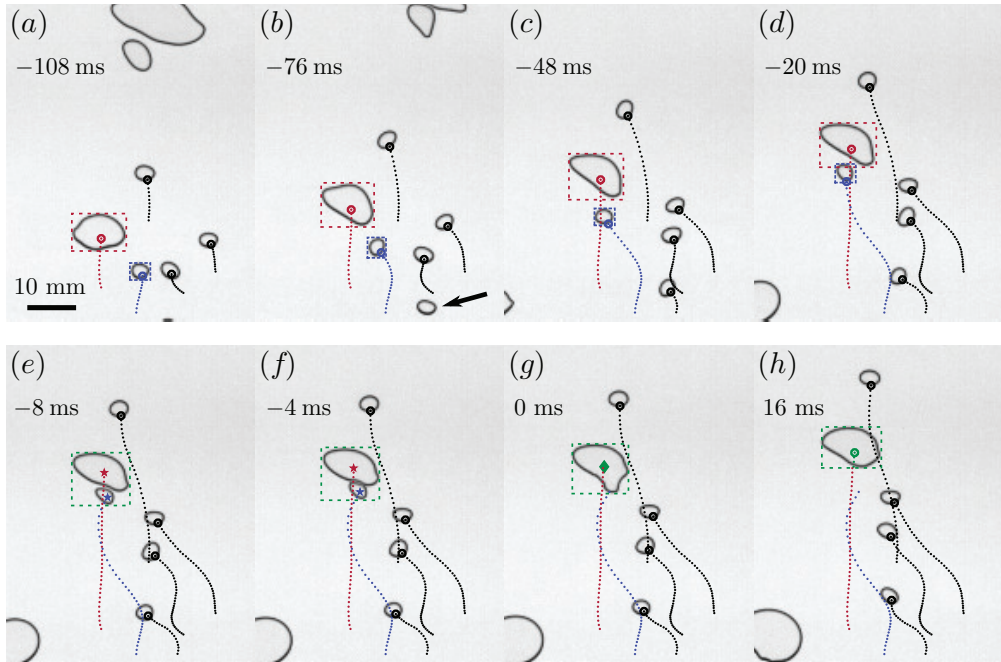


FIGURE 20. Characteristic sequence of the BTA performance showing the tracking process, superimposed on a region of the original grayscale images at different instants. The trajectories of the properly tracked bubbles are represented by a sequence of dots corresponding to the bubble centroid locations in the previous frames. (a-d) Examples of the correlation method applied to two different bubbles (red and blue, respectively), showing the positions of their centroids in the previous frame, $j - 1$, (circle) lying inside the corresponding bounding-box in frame j (dashed box). The black arrow in (b) indicates a new bubble entering the field of view. (e-f) Typical collision detected and tracked in two consecutive frames. The bounding-box of the bubble agglomerate is shown with a dashed dark green rectangle in each frame and the bubbles involved are marked with colored stars. (f-g) Sequence of the end of a collision event due to bubble coalescence. The parent bubbles (colored stars) give rise to a new bubble (green diamond). (h) The coalesced bubble is hereafter tracked as a single bubble (green circle).

981 edge width remains constant independently of the size of the colliding bubbles, this simple
 982 procedure allows us to avoid any further computation devoted to the separation of the
 983 bubbles, as occurs in more complicated 3D bubbly flows (see e.g. Rueda Villegas *et al.*
 984 2019).

985 A.2. Bubble Tracking and coalescence/breakage detection Algorithm (BTA)

986 The time evolution of each bubble in the swarm was obtained using a bubble tracking
 987 algorithm specifically designed and developed for this work, which includes a coales-
 988 cence/breakage detection algorithm, hereafter called BTA. It consists of the detection of
 989 the bubbles in a frame, j , followed by the search and identification of the same bubbles
 990 in the previous one, $j - 1$. For new bubbles, born in frame j either due to coalescence or
 991 breakup, family trees are established between the daughter (in frame j) and the parents
 992 (in frame $j - 1$).

993 More precisely, the algorithm involves a first step where an image (frame j) is processed
 994 using the digital analysis described in §A.1. As a result, the bubbles in the frame are
 995 detected, obtaining the positions of their centroids as well as their projected areas.

996 Afterwards, each bubble is classified as *single* or *in-collision* bubble. In addition to
997 the bubbles, the detected collisions, defined as agglomerates of two or more bubbles in
998 direct contact (see §A.1), are treated as independent entities and thus their characteristic
999 parameters are also calculated, including the total number of bubbles in collision. In order
1000 to facilitate the search of corresponding objects in two consecutive frames, a bounding-
1001 box containing the target object is defined for each bubble or agglomerate of bubbles
1002 (colliding bubbles). Figure 20 shows the BTA performance superimposed on the original
1003 grayscale image at various instants, being the reference time, $t = 0$, the frame where a
1004 coalescence event takes place (figure 20*g*). The trajectories of the bubbles are represented
1005 as a sequence of dots, which correspond to the locations of their centroids in the previous
1006 frames. The solid circles on each bubble denote the position of the centroid in the previous
1007 frame, $j - 1$. The above mentioned bounding-boxes are plotted in figures 20(*a-d*) for two
1008 different bubbles in red and blue respectively, while those corresponding to a collision
1009 event are shown in figures 20(*e, f*) in green. Notice that the bounding-box enclosing the
1010 collision becomes that of the newborn coalesced bubble in figure 20(*g*) since the collision
1011 event ends up with the coalescence of the two bubbles, as described in detail below.

1012 Once the bubbles in the images (frame j) have been detected, the key point of the
1013 tracking algorithm is to search for the corresponding ones in frame $j - 1$. In that sense,
1014 every single and in-collision bubble must be related, at least, to one object in the previous
1015 frame. Moreover, every detected collision must be related to a previous collision or, at
1016 least, to two previous bubbles. The procedure works sequentially identifying objects,
1017 taking into account the continuity of the bubbles trajectories and the conservation of
1018 volume (projected areas) of the objects. Initially, only single bubbles in both frames are
1019 considered. Therefore, a single bubble in frame j is related to the single one in frame
1020 $j - 1$ whose centroid falls inside the bounding-box of the bubble in frame j . Given the
1021 experimental acquisition rate, this bounding-box criteria is highly effective, even for the
1022 smallest bubbles that are accelerated when they are trapped in the wake of larger ones
1023 (figure 20*c, d*). However, when bubbles of very different sizes get closer (without being in
1024 contact), more than a centroid detected in frame $j - 1$ can be inside the bounding-box
1025 of the larger bubble in frame j . To avoid possible errors, an additional criterion based
1026 on the conservation of volume is imposed (Rodríguez-Rodríguez *et al.* 2003). Therefore,
1027 the volume of the corresponding bubbles in both frames must be equal. Bubbles located
1028 near the bottom edge of the field of view in frame j , which cannot be associated with
1029 any object in frame $j - 1$ (see e.g. the bubble highlighted by an arrow in figure 20*b*),
1030 are directly classified as new bubbles just entering the analysis region. Any other single
1031 bubble that cannot be related to a previous one is taken out for further analysis. The
1032 single bubbles properly tracked are stored in the data base and removed from both frames
1033 to facilitate the analysis of the colliding ones.

1034 The following step is devoted to the analysis of the agglomerates, which define collision
1035 events, detected in frame j . When several bubbles collide, the process can end with the
1036 bubbles coalescing or bouncing off each other. Thus, every collision detected in frame
1037 j , considered as an unique object, is analyzed searching for the corresponding collision
1038 object in frame $j - 1$, applying the algorithm described above to track individual bubbles.
1039 In addition to the volume of the agglomerate, the number of bubbles involved in the
1040 collision must also be conserved in both frames. If the corresponding collision is found in
1041 the previous frame, the bubbles that form the agglomerate (bubbles marked with colored
1042 stars in figure 20*e, f*) are identified as well using the criteria used for single bubbles. On
1043 the other hand, if no corresponding collision is found in frame $j - 1$, it is assumed that
1044 the collision detected in frame j is a new one occurring because several bubbles (usually
1045 two) have been brought together (figure 20*e*). In that case, the bubbles involved in the

collision are analyzed searching for the corresponding previous single bubbles leading to the collision. Once they have been processed, the agglomerates, as well as all the involved bubbles, are stored and no further action is performed with them in the current frame.

At this point, the remaining bubbles in frame j are those emerging either from the breakup of a mother bubble in frame $j - 1$ or from the *death* of a previous agglomerate. The latter gives rise to two different situations: (i) death by coalescence of the bubbles which form the agglomerate, creating a new larger bubble, or (ii) death by the separation of the involved bubbles, leading to different single bubbles in frame j . These two possibilities represent the basis of the collision efficiency concept. In (i) the collision results *efficient*, giving rise to a coalescence event. On the other hand, (ii) indicates an *inefficient* collision, where the involved bubbles continue living without changes in the population. To determine this efficiency, it has to be pointed out that both situations respectively arise from a collision detected in frame $j - 1$ which does not have a corresponding agglomerate in frame j . Therefore, a forward analysis, from frame $j - 1$ to frame j , is applied to the remaining agglomerates in frame $j - 1$. In this case, the correlation method used to track a single bubble is applied here for each bubble involved in the collision detected in frame $j - 1$, searching for the corresponding bubble in frame j . Only the remaining bubbles in frame j whose centroid falls inside the bounding-box of the analyzed agglomerate in frame $j - 1$, are considered. If the death of the collision is due to separation, any bubble forming the agglomerate in frame $j - 1$ will be related to a corresponding single bubble in frame j , satisfying both the bubble bounding-box as well as the bubble volume conservation criteria. However, if the collision event ends up in a coalescence, the bubble emerging from the coalescence is determined as the single bubble in frame j whose centroid falls inside the bounding-box of the analyzed agglomerate in frame $j - 1$, being its projected area equal to the sum of those of the parent bubbles. A typical coalescence event is shown in figure 20(*f, g*). The parent bubbles involved in the collision can be seen in frame $j - 1$ (figure 20*f*), being their centroids indicated by colored stars, while the newborn bubble is shown in frame j (figure 20*g*), with its centroid marked with a green diamond. From this point, the new bubble generated by coalescence is tracked as a single bubble (figure 20*h*).

Finally, the daughter bubbles remaining in frame j , which are generated due to the breakup of a mother bubble in frame $j - 1$, are identified through a backward-forward implementation of the correlation method, following the ideas proposed by Rodríguez-Rodríguez *et al.* (2003). For a potential daughter bubble in frame j , the corresponding mother bubble is searched in frame $j - 1$ as the larger bubble whose bounding-box includes the centroid of the analyzed daughter one. Then, the second daughter bubble is additionally searched in frame j as that whose centroid falls inside the bounding-box of the mother one and whose volume corresponds to the volume of the mother minus that of the sibling one. Therefore, both daughter bubbles in frame j are identified as new single bubbles appearing due to breakup, while the corresponding mother bubble in frame $j - 1$ is defined as *death* due to breakup.

REFERENCES

- ALMÉRAS, E., CAZIN, S., ROIG, V., RISSO, F., AUGIER, F. & PLAIS, C. 2016 Time-resolved measurement of concentration fluctuations in a confined bubbly flow by LIF. *Int. J. Multiphase Flow* **83**, 153–161.
- ALMÉRAS, E., RISSO, F., ROIG, V., PLAIS, C. & AUGIER, F. 2018 Mixing mechanism in a two-dimensional bubble column. *Phys. Rev. Fluids* **3** (7), 074307.
- ANTHONY, C. R., KAMAT, P. M., THETE, S. S., MUNRO, J. P., LISTER, J. R., HARRIS, M. T.

- 1093 & BASARAN, O. A. 2017 Scaling laws and dynamics of bubble coalescence. *Phys. Rev.*
1094 *Fluids* **2** (8), 083601.
- 1095 BONGIOVANNI, C., DOMINGUEZ, A. & CHEVAILLIER, J.-P. 2000 Understanding images of
1096 bubbles. *Eur. J. Phys.* **21** (6), 561.
- 1097 BOUCHE, E., CAZIN, S., ROIG, V. & RISSO, F. 2013 Mixing in a swarm of bubbles rising in a
1098 confined cell measured by mean of PLIF with two different dyes. *Exp. in Fluids* **54**, 1552.
- 1099 BOUCHE, E., ROIG, V., RISSO, F. & BILLET, A. M. 2012 Homogeneous swarm of high-Reynolds-
1100 number bubbles rising within a thin gap. Part 1. Bubble dynamics. *J. Fluid Mech.* **704**,
1101 211–231.
- 1102 BOUCHE, E., ROIG, V., RISSO, F. & BILLET, A. M. 2014 Homogeneous swarm of high-Reynolds-
1103 number bubbles rising within a thin gap. Part 2. Liquid dynamics. *J. Fluid Mech.* **758**,
1104 508–521.
- 1105 BUSH, J. W. M. & EAMES, I. 1998 Fluid displacement by high Reynolds number bubble motion
1106 in a thin gap. *Int. J. Multiphase Flow* **24** (3), 411–430.
- 1107 CHANDRASEKHAR, S. 1943 Stochastic problems in physics and astronomy. *Rev. Mod. Phys*
1108 **15** (1), 1.
- 1109 CHESTERS, A. K. 1991 Modelling of coalescence processes in fluid-liquid dispersions: a review
1110 of current understanding. *Chem. Eng. Res. Des.* **69** (A4), 259–270.
- 1111 CHESTERS, A. K. & HOFMAN, G. 1982 Bubble coalescence in pure liquids. *Appl. Sci. Res.* **38**,
1112 353–361.
- 1113 COLOMBET, D., LEGENDRE, D., RISSO, F., COCKX, A. & GUIRAUD, P. 2015 Dynamics and
1114 mass transfer of rising bubbles in a homogenous swarm at large gas volume fraction. *J.*
1115 *Fluid Mech.* **763**, 254–285.
- 1116 COULALOGLOU, C. A. & TAVLARIDES, L. L. 1977 Description of interaction processes in agitated
1117 liquid-liquid dispersions. *Chem. Eng. Sci.* **32** (11), 1289–1297.
- 1118 DEANE, G. B. & STOKES, M. D. 2002 Scale dependence of bubble creation mechanisms in
1119 breaking waves. *Nature* **418**, 839–844.
- 1120 DUINEVELD, P. C. 1998 Bouncing and coalescence of bubble pairs rising at high Reynolds
1121 number in pure water or aqueous surfactant solutions. *Appl. Sci. Res.* **58** (1), 409–439.
- 1122 EGGERS, J., LISTER, J. R. & STONE, H. A. 1999 Coalescence of liquid drops. *J. Fluid Mech.*
1123 **401**, 293–310.
- 1124 FIGUEROA-ESPINOZA, B., MENA, B., AGUILAR-CORONA, A. & ZENIT, R. 2018 The lifespan of
1125 clusters in confined bubbly liquids. *Int. J. Multiphase Flow* **106**, 138–146.
- 1126 FIGUEROA-ESPINOZA, B. & ZENIT, R. 2005 Clustering in high Re monodispersed bubbly flows.
1127 *Phys. Fluids* **17** (9), 091701.
- 1128 FILELLA, A., ERN, P. & ROIG, V. 2015 Oscillatory motion and wake of a bubble rising in a
1129 thin-gap cell. *J. Fluid Mech.* **778**, 60–88.
- 1130 FILELLA, A., ERN, P. & ROIG, V. 2020 Interaction of two oscillating bubbles rising in a thin-gap
1131 cell: vertical entrainment and interaction with vortices. *J. Fluid Mech.* **888**, A13.
- 1132 FRIEDLANDER, S. K. 1977 *Smoke, dust and haze*. Wiley, New York.
- 1133 FU, Y. & LIU, Y. 2016 Development of a robust image processing technique for bubbly flow
1134 measurement in a narrow rectangular channel. *Int. J. Multiphase Flow* **84**, 217–228.
- 1135 GHOSH, P. 2009 Coalescence of bubbles in liquid. *Bubble Sci. Eng. Technol.* **1** (1-2), 75–87.
- 1136 GORDILLO, J. M., SEVILLA, A. & MARTÍNEZ-BAZÁN, C. 2007 Bubbling in a co-flow at high
1137 Reynolds numbers. *Phys. Fluids* **19** (7), 077102.
- 1138 HASHIDA, M., HAYASHI, K. & TOMIYAMA, A. 2019 Rise velocities of single bubbles in a narrow
1139 channel between parallel flat plates. *Int. J. Multiphase Flow* **111**, 285–293.
- 1140 HINZE, J. O. 1955 Fundamentals of the hydrodynamic mechanism of splitting in dispersion
1141 processes. *AIChE J.* **1** (3), 289–295.
- 1142 HOWARTH, W. J. 1964 Coalescence of drops in a turbulent flow field. *Chem. Eng. Sci.* **19** (1),
1143 33–38.
- 1144 HUISMAN, S. G., ERN, P. & ROIG, V. 2012 Interaction and coalescence of large bubbles rising
1145 in a thin gap. *Phys. Rev. E* **85** (2), 027302.
- 1146 KAMP, A. M., CHESTERS, A. K., COLIN, C. & FABRE, J. 2001 Bubble coalescence in turbulent
1147 flows: a mechanistic model for turbulence-induced coalescence applied to microgravity
1148 bubbly pipe flow. *Int. J. Multiphase Flow* **27** (8), 1363–1396.

- 1149 KELLEY, ERIN & WU, MINGMING 1997 Path instabilities of rising air bubbles in a Hele-Shaw
1150 cell. *Phys. Rev. Lett.* **79** (7), 1265.
- 1151 KOCAMUSTAFAOGULLARI, G. & ISHII, M. 1995 Foundation of the interfacial area transport
1152 equation and its closure relations. *Int. J. Heat Mass Transfer* **38** (3), 481–493.
- 1153 KOLEV, N. I. 1993 Fragmentation and coalescence dynamics in multiphase flows. *Exp. Thermal
1154 Fluid Sci.* **6** (3), 211–251.
- 1155 LASHERAS, J. C., EASTWOOD, C. D., MARTÍNEZ-BAZÁN, C. & MONTAÑÉS, J. L. 2002 A
1156 review of statistical models for the break-up of an immiscible fluid immersed into a fully
1157 developed turbulent flow. *Int. J. Multiphase Flow* **28** (2), 247–278.
- 1158 LIAO, Y. & LUCAS, D. 2009 A literature review of theoretical models for drop and bubble
1159 breakup in turbulent dispersions. *Chem. Eng. Sci.* **64** (15), 3389–3406.
- 1160 LIAO, Y. & LUCAS, D. 2010 A literature review on mechanisms and models for the coalescence
1161 process of fluid particles. *Chem. Eng. Sci.* **65** (10), 2851–2864.
- 1162 LUNDIN, M. D. & MCCREADY, M. J. 2009 Modeling of bubble coalescence in bubbly co-current
1163 flows restricted by confined geometry. *Chem. Eng. Sci.* **64** (18), 4060–4067.
- 1164 MARCHISIO, D. L. & FOX, R. O. 2013 *Computational models for polydisperse particulate and
1165 multiphase systems*. Cambridge University Press.
- 1166 MARRUCCI, G. 1969 A theory of coalescence. *Chem. Eng. Sci.* **24** (6), 975–985.
- 1167 MARTÍNEZ-BAZÁN, C. 1999 Splitting and dispersion of bubbles by turbulence. PhD thesis,
1168 University of California San Diego, USA.
- 1169 MARTÍNEZ-BAZÁN, C., MONTAÑÉS, J. L. & LASHERAS, J. C. 1999a On the breakup of an air
1170 bubble injected into a fully developed turbulent flow. Part 1. Breakup frequency. *J. Fluid
1171 Mech.* **401**, 157–182.
- 1172 MARTÍNEZ-BAZÁN, C., MONTAÑÉS, J. L. & LASHERAS, J. C. 1999b On the breakup of an air
1173 bubble injected into a fully developed turbulent flow. Part 2. Size PDF of the resulting
1174 daughter bubbles. *J. Fluid Mech.* **401**, 183–207.
- 1175 MARTÍNEZ-BAZÁN, C., RODRÍGUEZ-RODRÍGUEZ, J., DEANE, G. B., MONTAÑÉS, J. L. &
1176 LASHERAS, J. C. 2010 Considerations on bubble fragmentation models. *J. Fluid Mech.*
1177 **661**, 159–177.
- 1178 MARTINEZ MERCADO, J., CHEHATA, D., VAN GILS, D., SUN, C. & LOHSE, D. 2010 On bubble
1179 clustering and energy spectra in pseudo-turbulence. *J. Fluid Mech.* **650**, 287–306.
- 1180 MIYAHARA, T., TSUCHIYA, K. & FAN, L.-S. 1991 Effect of turbulent wake on bubble–bubble
1181 interaction in a gas–liquid–solid fluidized bed. *Chem. Eng. Sci.* **46** (9), 2368–2373.
- 1182 MORENO SOTO, A., MADDALENA, T., FRATERS, A., VAN DER MEER, D. & LOHSE, D. 2018
1183 Coalescence of diffusively growing gas bubbles. *J. Fluid Mech.* **846**, 143–165.
- 1184 NÉEL, B. & DEIKE, L. 2021 Collective bursting of free-surface bubbles, and the role of surface
1185 contamination. *J. Fluid Mech.* **917**, A46.
- 1186 NEITZEL, G. P. & DELL'AVERSANA, P. 2002 Noncoalescence and nonwetting behavior of liquids.
1187 *Annu. Rev. Fluid Mech.* **34** (1), 267–289.
- 1188 OELGEMOLLER, M. 2016 Solar photochemical synthesis: from the beginnings of organic
1189 photochemistry to the solar manufacturing of commodity chemicals. *Chem. Rev.* **116** (17),
1190 9664–9682.
- 1191 OOLMAN, T. O. & BLANCH, H. W. 1986 Bubble coalescence in stagnant liquids. *Chem. Eng.
1192 Commun.* **43**, 237–261.
- 1193 OTSU, N. 1979 A threshold selection method from gray-level histograms. *IEEE Trans. SMC*
1194 **9** (1), 62–66.
- 1195 PAULSEN, J. D., CARMIGNIANI, R., KANNAN, A., BURTON, J. C. & NAGEL, S. R. 2014
1196 Coalescence of bubbles and drops in an outer fluid. *Nat. Commun.* **5** (1), 1–7.
- 1197 PAVLOV, L., D'ANGELO, M. V., CACHILE, M., ROIG, V. & ERN, P. 2021 Kinematics of a
1198 bubble freely rising in a thin-gap cell with additional in-plane confinement. *Phys. Rev.
1199 Fluids* **6**, 093605.
- 1200 PIEDRA, S., RAMOS, E. & HERRERA, J. R. 2015 Dynamics of two-dimensional bubbles. *Phys.
1201 Rev. E* **91**, 063013.
- 1202 PRINCE, M. J. & BLANCH, H. W. 1990 Bubble coalescence and break-up in air-sparged bubble
1203 columns. *AIChE J.* **36** (10), 1485–1499.
- 1204 PRUVOST, J., LE BORGNE, F., ARTU, A. & LEGRAND, J. 2017 Development of a thin-film

- 1205 solar photobioreactor with high biomass volumetric productivity (AlgoFilm©) based on
1206 process intensification principles. *Algal Res.* **21**, 120–137.
- 1207 QI, Y., MASUK, A. U. M. & NI, R. 2020 Towards a model of bubble breakup in turbulence
1208 through experimental constraints. *Int. J. Multiphase Flow* **132**, 103397.
- 1209 RAMKRISHNA, D. 2000 *Population balances: Theory and applications to particulate systems in*
1210 *engineering*. Elsevier.
- 1211 RODRÍGUEZ-RODRÍGUEZ, J., MARTÍNEZ-BAZÁN, C. & MONTAÑÉS, J. L. 2003 A novel particle
1212 tracking and break-up detection algorithm: application to the turbulent break-up of
1213 bubbles. *Meas. Sci. Technol.* **14** (8), 1328.
- 1214 ROIG, V., ROUDET, M., RISSO, F. & BILLET, A. M. 2012 Dynamics of a high-Reynolds-number
1215 bubble rising within a thin gap. *J. Fluid Mech.* **707**, 444–466.
- 1216 ROUDET, M., BILLET, A. M., CAZIN, S., RISSO, F. & ROIG, V. 2017 Experimental investigation
1217 of interfacial mass transfer mechanisms for a confined high-Reynolds-number bubble rising
1218 in a thin gap. *AIChE J.* **63** (6), 2394–2408.
- 1219 RUEDA VILLEGAS, L., COLOMBET, D., GUIRAUD, P., LEGENDRE, D., CAZIN, S. & COCKX,
1220 A. 2019 Image processing for the experimental investigation of dense dispersed flows:
1221 application to bubbly flows. *Int. J. Multiphase Flow* **111**, 16–30.
- 1222 RUIZ-RUS, J. 2019 Controlled formation of bubbles and analysis of their collective dynamics.
1223 PhD thesis, Universidad de Jaén, Spain.
- 1224 SANADA, T., WATANABE, M., FUKANO, T. & KARIYASAKI, A. 2005 Behavior of a single coherent
1225 gas bubble chain and surrounding liquid jet flow structure. *Chem. Eng. Sci.* **60** (17), 4886–
1226 4900.
- 1227 SMOLUCHOWSKI, M. V. 1917 Versuch einer mathematischen Theorie der Koagulationskinetik
1228 kolloider Lösungen. *Z. Physik Chem.* **92** (2), 129–168.
- 1229 SOLIGO, G., ROCCON, A. & SOLDATI, A. 2019 Breakage, coalescence and size distribution of
1230 surfactant-laden droplets in turbulent flow. *J. Fluid Mech.* **881**, 244–282.
- 1231 SOVOVA, H. 1981 Breakage and coalescence of drops in a batch stirred vessel—II comparison of
1232 model and experiments. *Chem. Eng. Sci.* **36** (9), 1567–1573.
- 1233 THOBIE, C., GADOIN, E., BLEL, W., PRUVOST, J. & GENTRIC, C. 2017 Global characterization
1234 of hydrodynamics and gas-liquid mass transfer in a thin-gap bubble column intended for
1235 microalgae cultivation. *Chem. Eng. Process.* **122**, 76–89.
- 1236 TSOURIS, C. & TAVLARIDES, L. L. 1994 Breakage and coalescence models for drops in turbulent
1237 dispersions. *AIChE J.* **40** (3), 395–406.
- 1238 VINCENTI, W. G. & KRUGER, C. H. 1965 *Introduction to physical gas dynamics*. Wiley, New
1239 York.
- 1240 WANG, T. F., WANG, J. F. & JIN, Y. 2003 A novel theoretical breakup kernel function for
1241 bubbles/droplets in turbulent flows. *Chem. Eng. Sci.* **58**, 4629–4637.
- 1242 WILLIAMS, F. A. 1985 *Combustion theory*. Addison-Wesley, Redwood City, CA.
- 1243 ZHANG, F. H. & THORODDSEN, S. T. 2008 Satellite generation during bubble coalescence. *Phys.*
1244 *Fluids* **20** (2), 022104.